Polar wind survey with the Thermal Ion Dynamics Experiment/Plasma Source Instrument suite aboard POLAR

Yi-Jiun Su,[1,2] J. L. Horwitz,[1] T. E. Moore,[3] B. L. Giles,[3] M. O. Chandler,[4]

P. D. Craven,[4] M. Hirahara,[5] and C. J. Pollock[6]

Abstract. In February 1996, the POLAR spacecraft was placed in an elliptical orbit with a 9 R_E geocentric distance apogee in the northern hemisphere and 1.8 R_E perigee in the southern hemisphere. The Thermal Ion Dynamics Experiment (TIDE) on POLAR has allowed sampling of the three-dimensional ion distribution functions with excellent energy, angular, and mass resolution. The Plasma Source Instrument (PSI), when operated, allows sufficient diminution of the electric potential to observe the polar wind at very high altitudes. In this paper, we describe the results of a survey of the polar wind characteristics for H^+, He^+, and O^+ as observed by TIDE at ~5000 km and ~8 R_E altitudes over the polar cap during April-May 1996. At 5000 km altitude, the H^+ polar wind exhibits a supersonic outflow, while O^+ shows subsonic downflow, which suggests a cleft ion fountain origin for the O^+ ions in the polar cap region. Dramatic decreases of the 5000 km altitude H^+ and O^+ ion densities and fluxes are seen as the solar zenith angle increases from 90° to 100° for the ionospheric base, which is consistent with solar illumination ionization control. However, the polar cap downward O^+ flow and density decline from dayside to nightside in magnetic coordinates suggest a cleft ion fountain origin for the polar cap O^+. Cleft ion fountain origin O^+ density plumes could also be partially responsible for a similar day-night asymmetry in H^+, owing to the charge-exchange reaction. At 8 R_E altitude, both H^+ and O^+ outflows are supersonic and H^+ is the highly dominant ion species. The average bulk ion field-aligned velocities are in the typical ratio $V_{O+} : V_{He+} : V_{H+} \sim 2 : 3 : 5$, which may suggest a tendency toward comparable energy gains, such as via an electric potential layer.

1. Introduction

The polar wind is an ambipolar outflow of thermal plasma from the terrestrial ionosphere at high latitude to the magnetosphere along geomagnetic field lines, consisting mainly of H^+, O^+, and He^+ ions and electrons. Understanding the characteristics of the polar wind is important for many reasons. For example, the ionosphere serves as a primary source of magnetospheric plasma [*Horwitz*, 1982, 1987, 1995; *Shelley et al.*, 1982; *Moore et al.*, 1986a, b; *Chappell et al.*, 1987; *Moore and Delcourt*, 1995; *Ganguli*, 1996; *Horwitz and Moore*, 1997], and the polar wind is a principal means by which the ionospheric plasma is transported to the magnetosphere. Various characteristics of the polar wind have been modeled using hydrodynamic, generalized transport, kinetic, semikinetic, hybrid, and time-dependent approaches [e.g., *Banks and Hol-*

[1]Center for Space Plasma and Aeronomic Research, The University of Alabama in Huntsville, Huntsville, Alabama.
[2]Now at Space and Atmospheric Sciences, Los Alamos National Laboratory, Los Alamos, New Mexico.
[3]Laboratory for Extraterrestrial Physics, Goddard Space Flight Center, Greenbelt, Maryland.
[4]Space Sciences Laboratory, Marshall Space Flight Center, Huntsville, Alabama.
[5]Department of Physics, Rikkyo University, Tokyo, Japan.
[6]Instrumentation and Space Research Division, Southwest Research Institute, San Antonio, Texas.

zer, 1969; *Dessler and Cloutier*, 1969; *Raitt et al.*, 1975; *Schunk and Watkins*, 1981, 1982; *Horwitz and Lockwood*, 1985; *Gombosi et al.*, 1985; *Ganguli et al.*, 1987; *Gombosi and Schunk*, 1988; *Swift*, 1990; *Wilson et al.*, 1990; *Wilson*, 1992; *Demars and Schunk*, 1994; *Horwitz et al.*, 1994; *Tam et al.*, 1995; *Schunk and Sojka*, 1997; *Demars et al.*, 1998; *Su et al.*, 1998].

Direct observations of the polar wind were first made by Explorer 31 for the altitude range 500 to 3000 km [*Hoffman*, 1970; *Brinton et al.*, 1971; *Hoffman et al.*, 1974]. These data showed H^+ ion flow velocities of up to 10 km s^{-1} parallel to the geomagnetic field and outward flux levels of the order of 10^8 cm^{-2} s^{-1} above 2500 km. Polar wind observations from ISIS 2 (in a circular polar orbit at 1400 km) [*Hoffman and Dodson*, 1980] confirmed that an upward flow of both H^+ and He^+ ions exists over the polar cap. H^+ fluxes between 10^7 and 10^8 cm^{-2} s^{-1} were observed, and O^+ was found to be the dominant ion species at 1400 km altitude, where strong H^+ flows occur. H^+ flows along high-latitude field lines showing supersonic characteristics (the Mach number ranged from 2.6 to 5.1) at 2 R_E were observed for the first time by the retarding ion mass spectrometer (RIMS) on Dynamics Explorer (DE) 1 [*Nagai et al.*, 1984; *Olsen et al.*, 1986], in general accord with classical polar wind model results. Observed H^+ flux values mapped to 1000 km were ~2.6 × 10^8 cm^{-2} s^{-1} for disturbed conditions ($Kp=5-$).

High-altitude observations by the DE 1 high altitude plasma instrument (HAPI) over polar regions indicated that the polar outflow consists of two ion components [*Gurgiolo and Burch*, 1982]. One unheated component is the "classical"

polar wind; the other component involves perpendicular ion heating over the cusp and possibly in the polar cap. The altitude at which the heating occurred was estimated to lie between 8000 and 12,000 km. In addition to the classical polar wind, *Shelley et al.* [1982] have reported the existence of O^+-dominated, upward flowing ion events (with ~ 10% H^+) over the polar cap in the energy range from 0 to 100 eV above the spacecraft potential using the DE 1 energetic ion composition spectrometer (EICS) and further estimated that these ion outflow fluxes with an order of 10^6 cm^{-2} s^{-1} at 4.6 R_E (DE 1 apogee) were most likely the source of the tail lobe ion streams. A statistical study using DE 1 EICS data [*Yau et al.*, 1984] confirmed the importance of low-energy outflow of O^+ over the high-altitude polar cap.

Waite et al. [1985] have reported several distinguishing characteristics of O^+ outflows from DE 1 observations between October 7 and November 26, 1981. The low-energy O^+ outflow (2 to 10 eV) was a long-duration outflow at high altitudes over most of the polar cap during active magnetic conditions. The field-aligned distribution had a low temperature, 2000 to 5000 K, a fairly large drift velocity of 5 to 15 km s^{-1}, and a large flux ranging from 10^6 to 10^7 cm^{-2} s^{-1}, corresponding to about 5×10^7 to 5×10^8 cm^{-2} s^{-1} mapped downward along the diverging magnetic field to the ionosphere. The observations of *Waite et al.* [1985] also pointed to the cleft region as a source of O^+ to the high-altitude polar cap. It was noted that the cleft or cusp represents a strong source of upflowing ions, particularly O^+, over the polar cap region [*Lockwood et al.*, 1985a, b]. With low-energy ion measurements (RIMS) on the DE 1 satellite, *Lockwood et al* [1985b] concluded that upwelling ions at the cleft form an ion fountain and are blown into the polar cap by antisunward convection. The transport of ionospheric ions from a source in the polar cleft ionosphere through the polar magnetosphere was investigated using a two-dimensional, kinetic, trajectory-based code by *Horwitz and Lockwood* [1985]. Their resulting plasma distributions and parameters are in general agreement with low-energy ion measurements (RIMS) [*Lockwood et al.*, 1985b]. *Pollock et al.* [1990] found that the upwelling plasma below 3 R_E is rich in O^+, which typically comprises about 90% of the ion density in the dayside cleft region for spring conditions during an active portion of the solar cycle. The typical upwelling O^+ ion flux from *Pollock et al.* [1990] was ~ 6×10^8 cm^{-2} s^{-1} (mapped to an altitude of 1000 km). There is, however, no clear-cut relationship between either the occurrence or intensity of upwelling ion events and the immediately preceding hourly averaged value of the interplanetary magnetic field (IMF) B_z component.

Observations of H^+, He^+, and O^+ with energies down to spacecraft potential were reported by *Chandler et al.* [1991], whose data set encompassed the period from autumn 1981 through 1983 between the altitude of 1000 and 4000 km at invariant latitudes greater than 70°. They showed that the average density of each ion species decreases with altitude. In the altitude range 1000 to 4000 km, O^+ is always the dominant ion (10^3 cm^{-3}), with an H^+ density of ~ 100 cm^{-3} and He^+ density of ~ 10 cm^{-3}. The H^+ velocity increased from 4 to 10 km s^{-1} over the altitude range 1000 to 4000 km. Observations of the H^+, He^+, and O^+ polar wind ions in the polar cap (> 80° invariant latitude (ILT)) from 2000 to 10,000 km altitude from Akebono were reported by *Abe et al.* [1993a, b]; both the ion parallel velocity and temperature distributions exhibited a day-to-night asymmetry, showing higher average values of parallel velocities and temperatures on the dayside than on the nightside. For all three ion species, the parallel ion velocity increased with altitude. The average H^+ velocity reached 1 km s^{-1} near 2000 km, as did the He^+ velocity near 3000 km and the O^+ velocity near 6000 km. At Akebono apogee (10,000 km), the average H^+, He^+, and O^+ velocities were near 12, 7, and 4 km s^{-1}, respectively. DE 1 RIMS observations of O^+ velocities by *Chandler* [1995] showed both upward and downward O^+ flows at DE 1 apogee; the upflows occurred in the dayside cusp region and at auroral latitudes during all local times, while the downflows were restricted to the polar cap. Global ionosphere polar wind simulations by *Schunk and Sojka* [1997] presented similar results. The O^+ velocity field observed by *Chandler et al.* [1991] is consistent with a scenario that has O^+ of cusp/cleft and auroral zone origin convected into the polar cap and, because of the dominance of gravitational energy over the upward kinetic energy, falling back into the polar cap ionosphere [e.g., *Horwitz and Lockwood*, 1985].

The POLAR spacecraft was launched on February 24, 1996, into a 90° inclination, polar elliptical orbit with 9 R_E apogee geocentric distance in the northern hemisphere and 1.8 R_E perigee in the southern hemisphere [*Acuña et al.*, 1995]. The Thermal Ion Dynamics Experiment (TIDE) on POLAR samples the three-dimensional ion distributions once per 6 s spin of the spacecraft with excellent low energy, angular (22.5° polar angle resolution and 11.25° spin azimuth resolution), and mass resolution for the 0.3–450 eV energy range [*Moore et al.*, 1995]. The accompanying Plasma Source Instrument (PSI), when operated, allows sufficient diminution of the electric potential to observe the low-energy polar wind ions at very high altitudes [*Moore et al.*, 1997].

This paper presents a survey of the polar wind characteristics in the polar cap region near 5000 km altitude (perigee) in the southern hemisphere and 8 R_E altitude (apogee) in the northern hemisphere. The apogee measurements included were during the early portion (April–May) of the POLAR mission in 1996 when PSI was operating. We do not include data collected from June through July 1996 owing to unreliable calibrations during these periods. Beginning with August 1996, the TIDE time-of-flight (TOF) mass analyzer stopped functioning properly and could not distinguish the different ion species. In our survey, each sample is based on data accumulated over 1 min (10 spins).

A special analysis technique for ion bulk parameter estimates is described in the following section. Using this technique for the parameters, the general bulk parameter trends and averages for the 5000 km polar wind are presented in section 3. The relationships of ion bulk parameters with the solar zenith angle and with the day-night distance in the solar magnetic coordinate system at 5000 km altitude are also presented in section 3. In section 4, we show the polar wind characteristics and general trends in bulk parameters for POLAR apogee when PSI was operating. We summarize and discuss our polar wind survey in section 5.

2. Ion Bulk Parameter Analysis

In this paper, we only focus on the "quiet" polar wind, excluding the cusp/cleft region and auroral zone, which are distinguishable in the ion "chromograms." A typical example at POLAR perigee is shown in Plate 1, where the spacecraft passes through the auroral zone (0322–0327 UT), polar cap (0327–0342 UT), and cusp/cleft region (0342–0349 UT) on
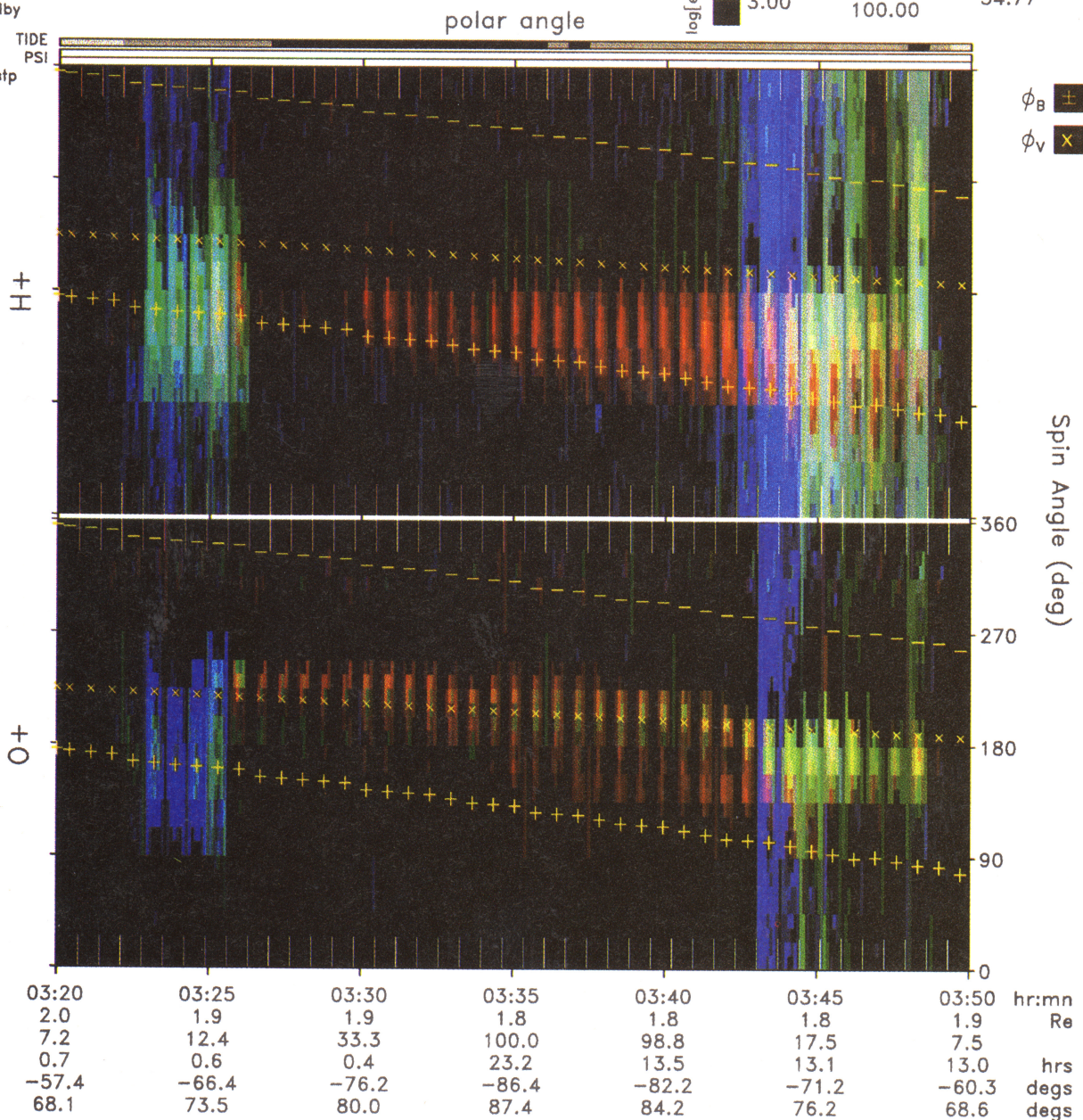
Plate 1. (top) H+ and (bottom) O+ ion flux data plotted after averaging over 42 s (seven spins) intervals, which are bounded by white tic marks at POLAR perigee from 0320 to 0350 UT on April 4, 1996. The energy flux is color coded (102 to 108 eV s-1 cm-2 sr-1 eV-1 as indicated by the vertical brightness bar) versus polar angle (0° to 157.5°), spin azimuth angle (0° to 360°, along the vertical axis), and energy. The color wheel indicates the interpretation of colors as energy distributions (red for the low energy from 0 to 3 V, green for the energy from 3 to 30 V, and blue for the high energy from 30 to 100 V). Universal time (UT), spacecraft geocentric radius (R_E), L shell (Lshell), magnetic local time (mlt), magnetic latitude (mlat), and invariant latitude (invlat) are indicated along the horizontal axis. The spin angle closest to the magnetic field direction and its opposite are indicated by pluses and minuses while the spacecraft velocity spin angle is indicated by crosses signs.

TIDE Phase Space Density Velocity Distribution Plots
04/23/96 03:34:57 to 03:35:56 UT

mag_el: 84°

mag_az: 271°

s/c pot: 1.73 0.20 v

gse_dec: 0.43 rad

gse_r_asc: 4.63 rad

Re: 1.8452

Lshell: 100.000

mlt: 8.1 hr

mlat: −86.957°

invlat: 87.782°

TIDE on, PSI off

Vsc−X:−2.49e−01 km/s

Vsc−Y: 7.49e+00 km/s

Vsc−Z:−9.70e−02 km/s

moments calculation ranges:
energy (RPA V): 0.00− 12.00
spin angle:180.00−247.50°
polar channels: 3−6

den: 7.96e+00 cm^{-3}

t_parl: 1.72e−01 eV

t_perp: 4.15e−01 eV

Vpl−X:−1.08e+00 km/s

Vpl−Y: 5.93e−02 km/s

Vpl−Z:−7.82e−01 km/s

earth
+ spacecraft
+ plasma

O+

Perpendicular Plane
Vx = −1.1 km/s
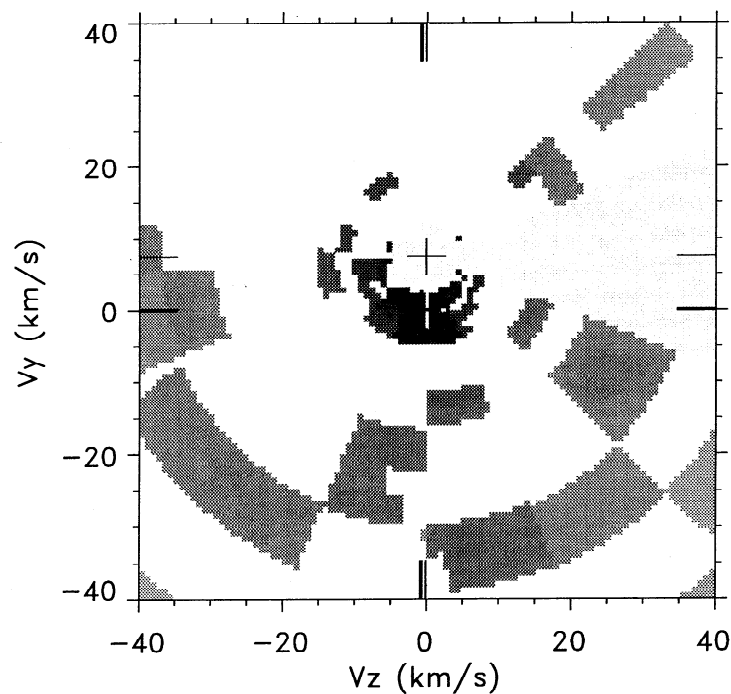
Parallel Plane
Vz = −0.8 km/s

SEC^3 KM^{-6}
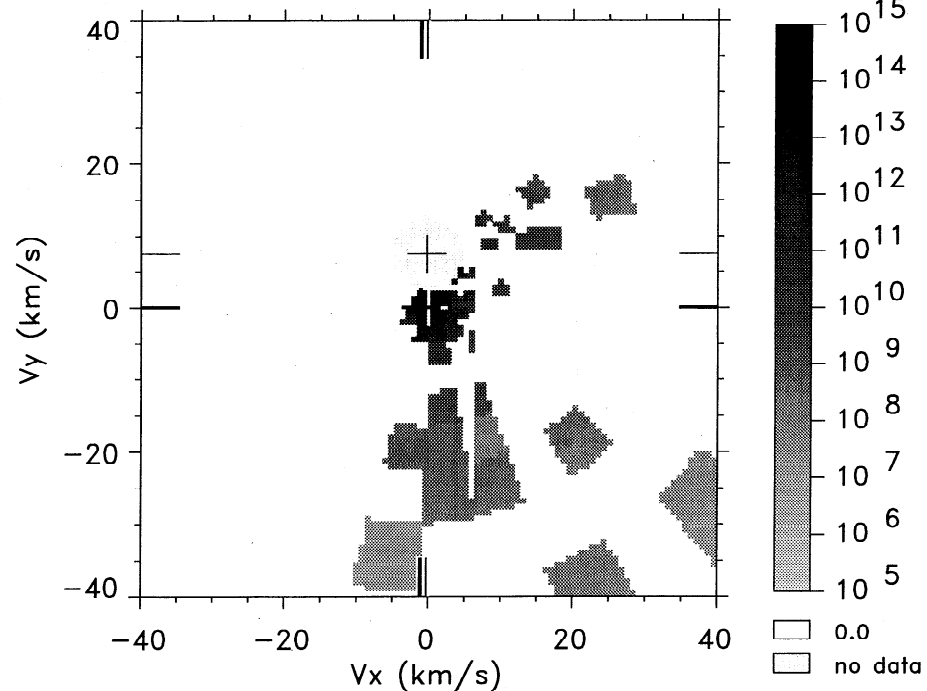
April 4, 1996. Our study here is restricted to low-energy ions (less than 10 V, seen as red in Plate 1), i.e., the polar wind, in the polar cap region and excludes data from the cusp/cleft and auroral regions. The H^+ ion flow peaks between the magnetic field line direction (pluses) and the ram direction (crosses) in Plate 1, top, while O^+ ions flow primarily along the ram direction in Plate 1, bottom. The additional counts seen between the magnetic field line and ram directions in Plate 1, bottom, are spurious signals resulting from H^+ ion counts in the O^+ channel, and are excluded from our analysis.

TIDE was designed to measure very low energy ions and was tested and calibrated with laboratory beams having energies down to 0.6 eV. However, the very lowest energy portion of the low-energy ion distributions, even at 5000 km altitude, is still shielded from the spacecraft (the spacecraft potential is usually $\geq$ 1.8 V). Typical O^+ and H^+ phase space density distributions at perigee are shown in Figures 1a and 1b from 0334:57 to 0335:36 UT (1 min average) on April 23, 1996, in which the x axis is defined by the local magnetic field, the y axis is defined by the normal vector lying in the spacecraft orbit plane, and the z axis is orthogonal to the x and y axis. In Figure 1a (left), the phase-spaced density distribution is sliced in the plane perpendicular to the local magnetic field for an O^+ velocity of $V_X = -1.1$ km s^{-1}. Figure 1a (right) shows a slice in the parallel plane with $V_Z = -0.8$ km s^{-1}. Likewise, a perpendicular plane of H^+ distribution with $V_X = 15.8$ km s^{-1} is seen in Figure 1b (left), while Figure 1b (right) shows a parallel plane with $V_Z = -4.5$ km s^{-1}. We note that the polar wind moments are only calculated by the restricted region in energy, spin azimuth, and polar angle as indicated on the plots. Only a relatively small region of velocity space (approximately the region of $V_x=[-8, 12]$, $V_y=[-10, 10]$, and $V_z=[-15, 10]$ km s^{-1} in Figure 1a, and the region of $V_x=[-12, 35]$, $V_y=[-20, 20]$, and $V_z=[-22, 25]$ km s^{-1} in Figure 1b) has been calculated, so that the outlying velocity space region does not contribute to the moments. The "standard" moment calculation does not include contributions from portions of the distributions reflected by the spacecraft potential (1.73 V for the case in Figures 1a and 1b). This shielding is especially severe for H^+ ions, leading to the crescent-shaped partial distribution in Figure 1b (right). Therefore we use an iterative bi-Maxwellian "filling" technique to fill in the three-dimensional distributions in order to obtain the improved bulk parameter estimates (described below). In addition, we have corrected for an anomalous enhancement in the low-energy channels (retarding potential analyzer (RPA) channels < 4 eV) for the polar sector 4 (67.5°–90°). We therefore substitute the average of measurements (for perigee only) from polar sectors 3 and 5 for those of (the abnormally high sensitivity) sector 4 before the

distribution filling-in process for our study. Twelve of the 31 energy bins for sector 4 were adjusted by this method.

The basic analysis approach with our filling-in procedure proceeded as follows: first, we localized our region of distribution function analysis in energy, spin azimuth, and polar angle to obtain a generally narrow ion beam, consisting only of the low-energy polar wind stream, among other reasons, in order to exclude "ghost peaks" (spurious signals resulting from other ion species) and "Sun pulses" (spurious counts associated with sunlight leaks) when calculating the moments. The original density, velocity, and temperature from the standard TIDE moment calculation are assumed as the initial input parameters to drive the iterative filling procedure. Using these initial moments, a drifting bi-Maxwellian distribution is generated and used to fill in the portion of the distribution that is shielded by the spacecraft potential. The drifting bi-Maxwellian is of the form

$$f = N\left(\frac{m}{2\pi kT_{\parallel}}\right)^{1/2}\left(\frac{m}{2\pi kT_{\perp}}\right)\bullet\exp\{-\frac{m(V_X - V_{Xo})^2}{2kT_{\parallel}}$$
$$-\frac{m\left[(V_Y - V_{Yo})^2 + (V_Z - V_{Zo})^2\right]}{2kT_{\perp}}\} \tag{1}$$

where m, k, N, $T_{\parallel}$, and $T_{\perp}$ are the ion mass, Boltzmann constant, density, and parallel and perpendicular temperatures, respectively. V_X, V_Y, and V_Z are the parallel velocity and two components of perpendicular velocities, respectively, where the x axis is the parallel magnetic field direction, the y axis is the normal direction lying in the spacecraft orbit plane, and the z axis is orthogonal to x and y axis. V_o indicates the bulk flow velocity. N, V_{Xo}, V_{Yo}, V_{Zo}, $T_{\parallel}$, and $T_{\perp}$ are supplied by the initial (or previous) moment calculation.

The new moments are calculated from the original distribution f_i for outside the shielded region and from the generated bi-Maxwellian distribution function for the originally shielded region. We then iterate this process until it converges, attaining a minimum deviation, $|f_i-f_{biM}(\Phi>\Phi_{sc})|_{minimum}$, or when the parameters remain stable under successive iterations. In this way, the actual measurements are always honored (outside the shielded region) while using them as the basis for estimating the "most likely" values for the region of velocity space that are obscured by the spacecraft potential. This special iterative filling-in procedure is summarized in the flow chart as shown in Figure 2.

At POLAR perigee, it is often found that more than 50% of the H^+ distribution appears to be shielded by the spacecraft potential. Reasonable initial input estimates are required; otherwise, the filling-in process will not converge. We first

Figure 1a. Typical phase space density velocity distribution for O^+ at perigee from 0334:57 to 0335:56 UT on April 23, 1996, where the x axis is the local magnetic field direction, the y axis is the normal vector lying in the spacecraft orbit plane, and the z axis is orthogonal to the x and y axis. The phase-spaced density distribution is sliced in the plane perpendicular to the local magnetic field for an O^+ velocity of $V_X = -1.1$ km s^{-1}. (right) Slice in the parallel plane with $V_Z = -0.8$ km s^{-1}. The phase-space density is contoured as indicated by the saturated gray-scale bar at right. The tic mark indicate the spacecraft frame of reference (thin black), the Earth frame of reference (white) and the computed plasma frame (thick black). The distributions are shielded by the spacecraft potential estimated to be 1.73 V here, especially the H^+ distributions in Figure 1b. The approximate region for the velocity space integration is discussed in the text.
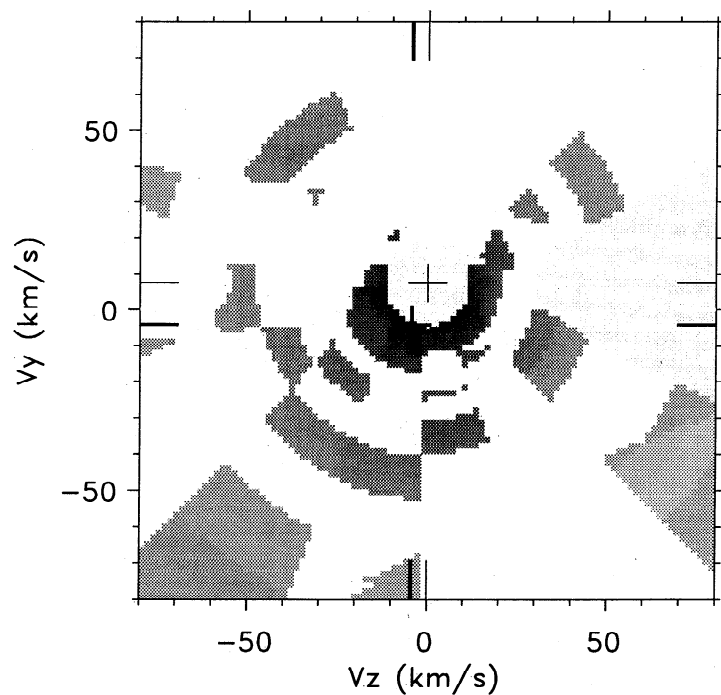
TIDE Phase Space Density Velocity Distribution Plots
04/23/96 03:34:57 to 03:35:56 UT

mag_el: 84°

mag_az: 271°

s/c pot: 1.73 0.20 v

gse_dec: 0.43 rad

gse_r_asc: 4.63 rad

Re: 1.8452

Lshell: 100.000

mlt: 8.1 hr

mlat: −86.957°

invlat: 87.782°

TIDE on, PSI off

Vsc−X:−2.49e−01 km/s

Vsc−Y: 7.49e+00 km/s

Vsc−Z:−9.70e−02 km/s

moments calculation ranges:

energy (RPA V): 0.00− 10.00

spin angle:225.00−315.00°

polar channels: 3−6

den: 4.80e+00 cm^{-3}

t_parl: 1.34e−01 eV

t_perp: 2.15e−01 eV

Vpl−X: 1.58e+01 km/s

Vpl−Y:−4.16e+00 km/s

Vpl−Z:−4.48e+00 km/s

earth

+ spacecraft

+ plasma

H+

Perpendicular Plane
Vx = 15.8 km/s

Parallel Plane
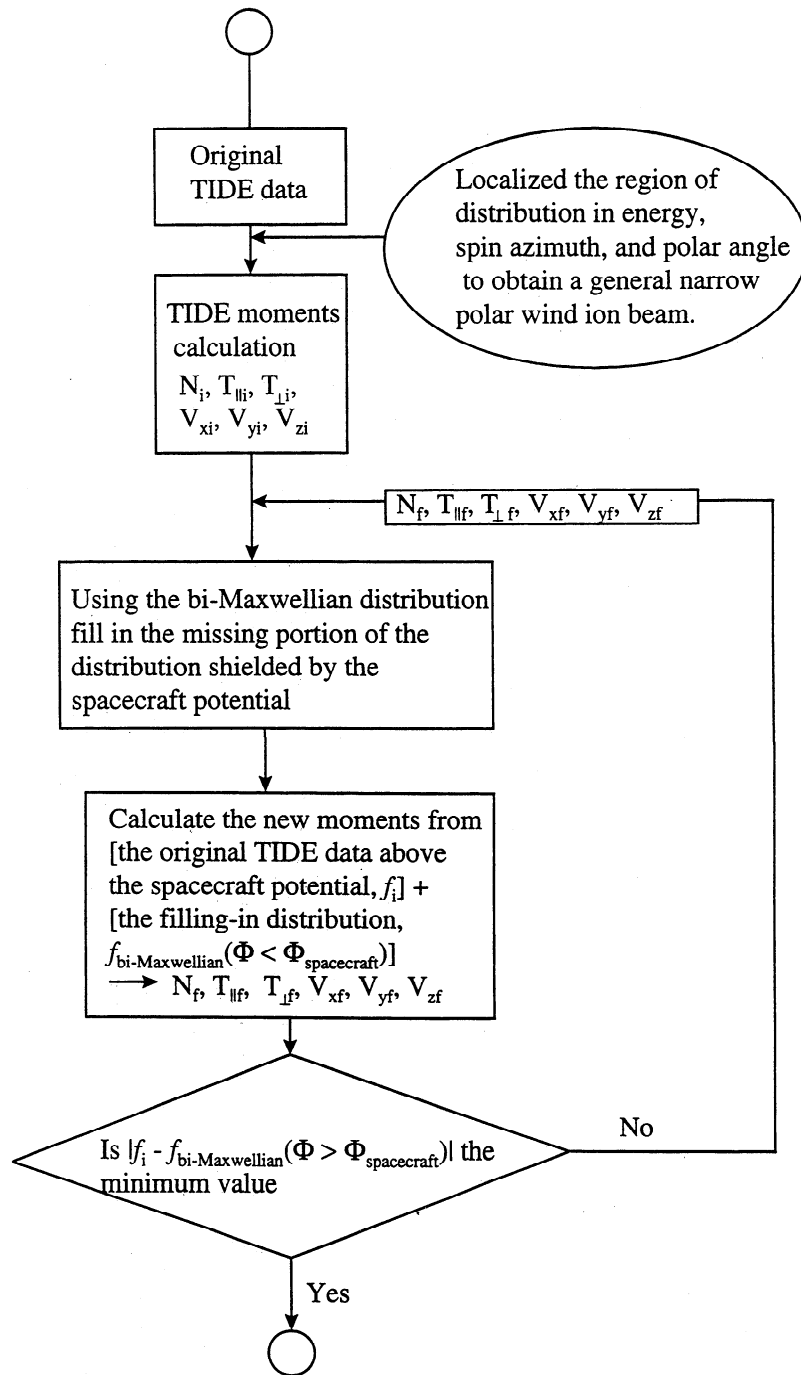Vz = −4.5 km/s

SEC^3 KM^{-6}
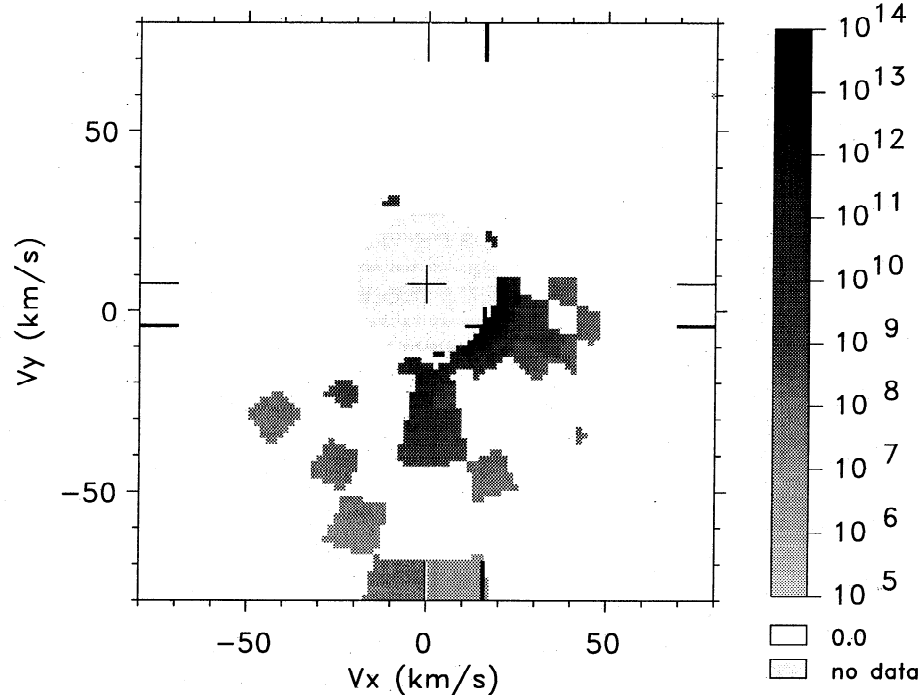
Figure 2. The flow chart of the bi-Maxwellian filling-in procedure.

used the process described above to fill in the O^+ distribution assuming that O^+ and H^+ have the same convection velocity. The resulting O^+ convection velocity is then assumed as the initial input convection velocity for H^+ distribution. To begin the iteration for the H^+ distribution moments, we used the higher density and temperatures from the original moment cal-

culation as the initial input parameters. After the iterative filling process, significantly more accurate ion densities, velocities, and temperatures are obtained. For O^+ distributions, the number of iterations is usually two or three until it reaches the minimum deviation. For H^+ distributions, the number of iterations, however, depends sensitively on the initial input esti-

Figure 1b. Same as Figure 1a., but for H^+. (left) A perpendicular plane of H^+ distribution with $V_X = 15.8$ km s^{-1} and (right) a parallel plane with $V_Z = -4.5$ km s^{-1}. The velocity and gray-scale bar ranges differ between the O^+ and H^+ panels. Note difference in the velocity and gray-scale bar ranges differ between Figures 1a and 1b.

Vsc–X : –2.49e–01 km/s
Vsc–Y : 7.49e+00 km/s
Vsc–Z : –9.70e–02 km/s
s/c pot : 1.73 v
mag_el : 84°
mag_az : 271°

momnets calculation ranges :
energy (RPA V) : 0. – 10.00
spin angle : 225.00 – 315.00
polar channels : 3 – 6

H+
4/23/96 03:34:57 – 03:35:56

den : 9.77e+00 cm^{-3}
t_parl : 1.52e–01 eV
t_perp : 2.39e–01 eV
Vpl–X : 1.21e+01 km/s
Vpl–Y : 2.27e–01 km/s
Vpl–Z : –7.92e–03 km/s

Vx = 15.8 km/s

Vz = –4.5 km/s

SEC^3 KM^{-6}

10^{14}
10^{13}
10^{12}
10^{11}
10^{10}
10^{9}
10^{8}
10^{7}
10^{6}
10^{5}

Vy (km/s)

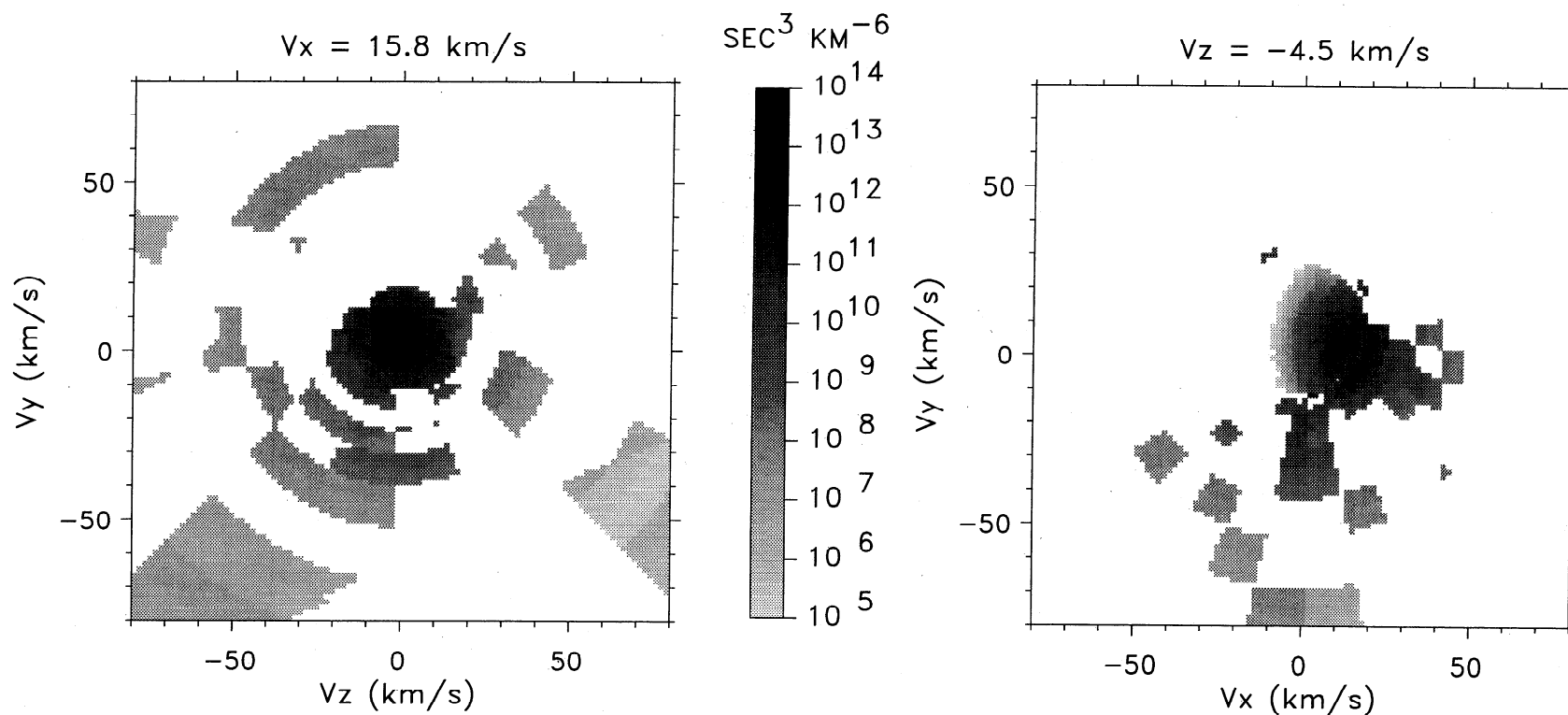Vz (km/s)

Vy (km/s)

Vx (km/s)

Figure 3. The H$^+$ phase space density velocity distribution after the iterated "filling" technique, starting from the distribution displayed in Figure 1b. The phase space density is contoured as indicated by the saturated gray-scale bar at center, which is the same gray-scale bar as in Figure 1b. Note that the moments are only calculated over the same region of velocity space as in Figure 1b, so that the outlying velocity space regions do not contribute to the moments.

TIDE Moments
start time: 04/20/96 05:13:35
stop time: 04/20/96 05:26:05
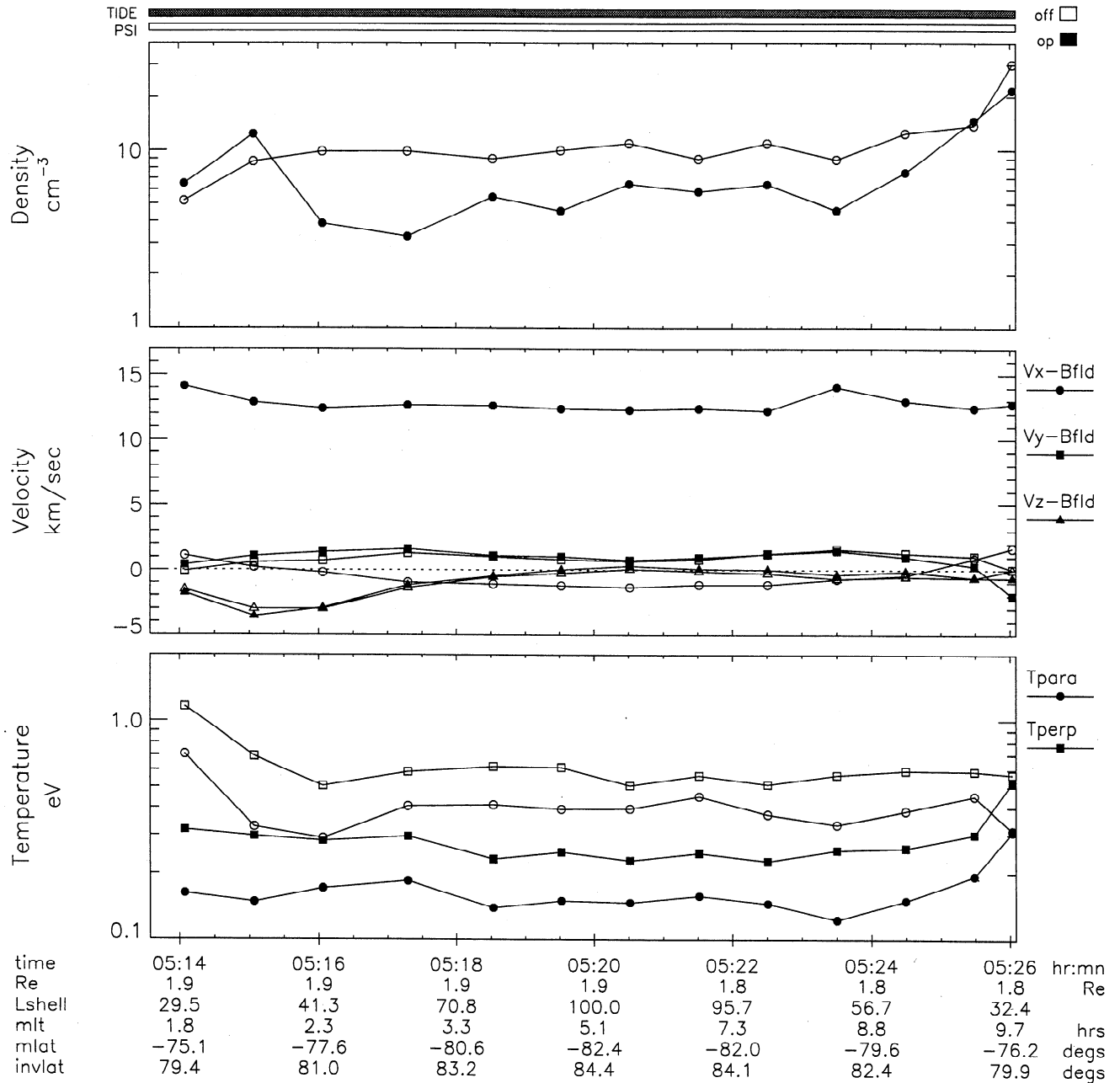s/c potential from file
10 spins averaged

O$^+$ open symbols ; H$^+$ closed symbols

mir stp ▦
standby ▨
off ☐
op ■

time	05:14	05:16	05:18	05:20	05:22	05:24	05:26	hr:mn
Re	1.9	1.9	1.9	1.9	1.8	1.8	1.8	Re
Lshell	29.5	41.3	70.8	100.0	95.7	56.7	32.4	
mlt	1.8	2.3	3.3	5.1	7.3	8.8	9.7	hrs
mlat	−75.1	−77.6	−80.6	−82.4	−82.0	−79.6	−76.2	degs
invlat	79.4	81.0	83.2	84.4	84.1	82.4	79.9	degs

Figure 4. H$^+$ and O$^+$ bulk parameters, including density, velocity along the local magnetic filed line V_X (circles), velocity of the normal vector lying in the spacecraft orbit plane V_Y (squares), velocity component orthogonal to x and y axis V_Z (triangles), and the temperatures parallel (circles) and perpendicular (squares) to the local magnetic field plotted at 1 min intervals using the analysis technique described in Figure 3, for one typical POLAR perigee pass from 0513:35–0526:05 UT on April 20, 1996. Universal time (UT), spacecraft geocentric radius (Re), L shell (Lshell), magnetic local time (mlt), magnetic latitude (mlat), and invariant latitude (invlat) are indicated along the horizontal axis. The open symbols represent the parameters for O$^+$ ions, while the solid symbols represent the parameters for H$^+$ ions.

mates of density and temperatures, which may be near or far from the final estimates. The iterative filling process improved the TIDE bulk parameter estimates, in particular, the H$^+$ and O$^+$ convection velocities that are in better agreement with each other.

Figure 3 shows the H$^+$ distribution after completing the filling process in both the parallel (right) and perpendicular planes (left) from 0334:57 to 0335:56 UT on April 23, 1996, starting from the original distribution shown in Figure 1b. Both density and temperature of the H$^+$ ions are seen to in-

crease relative to the unmodified moments after the filling process, while the parallel velocity is seen to decrease. For example, the original density, parallel and perpendicular temperatures, and velocities in x, y, and z components for the H^+ ion distribution are 4.8 cm^{-3}, 0.13 and 0.22 eV, and 15.8, −4.16, and −4.48 km s^{-1}, respectively, in Figure 1b. After the filling process, the new density, parallel and perpendicular temperatures, and velocities in x, y, and z components are 9.77 cm^{-3}, 0.15 and 0.24 eV, and 12.1, 0.23, and −0.008 km s^{-1} as seen in Figure 3.

Figure 4 shows typical O^+ (open symbols) and H^+ (solid symbols) polar wind bulk parameters for one perigee pass from 0513:35 to 0526:05 UT on April 20, 1996, based on the moments using the filling analysis. The O^+ density and temperature are larger than the H^+ density and temperature, in general. O^+ and H^+ convection velocities (Figure 4, middle, squares and triangles) generally tend to coincide when the H^+ densities are greater than 1 cm^{-3}, such as for the example in Figure 4. The polar wind characteristics at 5000 km altitude are discussed in section 3.

There are several origins of possible uncertainties in the presented parameters: (1) the Poisson statistics error estimation associated with the individual measurements (see *Moore et al.* [1996, appendix]); (2) the uncertainties due to using the average of the polar sectors 3 and 5 replacing sector 4 for the low-energy channels, which would become important if the distribution were a narrow beam centered on sector 4; (3) the uncertainties due to using the assumed bi-Maxwellian distribution to fill in the shielded region of velocity space; (4) the uncertainties associated with absolute calibration (for example, we may need to compare the densities measured by TIDE with possible density measurements by the plasma wave instrument (PWI) [*Gurnett et al.*, 1995] to recalibrate the countrate-flux conversion for the TIDE instruments); (5) the uncertainties due to geophysics fluctuations during the 1 min accumulation intervals. However, we believe that the polar wind characteristics described in this paper should be representative of the real polar wind attributes.

We do not have quantitative estimates for all the possible uncertainties at this time. Some of these uncertainties require further investigation. Here we only estimate the Poisson statistics based errors associated with the individual measurements based on *Moore et al.* [1996, appendix]. The fractional error in the density moments due to counting statistics is approximately equal to the fractional error of the highest phase space density in the distribution ($\sqrt{n}/n$, where n is the ion counts). For a typical POLAR perigee on April 23, 1996, the O^+ peak count samples were ≤1235 counts, so the uncertainty percentage above was ~ 2.85%. The H^+ peak count samples were ≤140 counts, so the uncertainty percentage is estimated as ~ 8.45%.

3. Survey of the 5000 km Altitude Polar Wind

The TIDE observations at POLAR perigee (~ 5000 km altitude) reported here were made over the southern polar cap. Excluding the cleft/cusp and auroral regions, we analyzed 20 perigee orbits of TIDE data in April 1996. Each sample data is averaged over 1 min. The moment calculations for the ion densities, velocities, and temperatures were based on the iterative filling techniques described in section 2. First, we discuss the relationship of the obtained polar wind parameters with solar zenith angle (SZA) and then present polar wind characteris-

tics and general trends in the obtained bulk parameters. We finally discuss the relationship of the bulk parameters with day-night distance in the solar magnetic (SM) coordinate system.

3.1. Relationship of Parameters at 5000 km Altitude With Solar Zenith Angle

Measurements from 5000 to 10,000 km altitude by the Akebono satellite have indicated higher polar wind velocities in the sunlit region than on the nightside [*Abe et al.*, 1993a]. Recent simulation results of the photoelectron-driven polar wind [*Su et al.*, 1998] have shown a dramatic decrease in the photoelectron number flux at 800 km altitude as the solar zenith angle increases from about 90° to 105°, which is shown in Figure 5, top. Using the same coupled fluid-semikinetic model, a plot of the O^+ density versus the solar zenith angle is shown Figure 5, bottom, at 500 km altitude, which also shows the O^+ densities decreasing with increasing solar zenith angle. These could suggest strong solar illumination ionization control of topside ionosphere densities in the polar cap. We therefore sought to relate polar wind characteristics from TIDE observations to the solar zenith angle.

Plots of the H^+ and O^+ densities, H^+ and O^+ parallel velocities, O^+/H^+ density ratio, and H^+ and O^+ number fluxes from TIDE versus solar zenith angle are shown in Figures 6a–6g, respectively. In Figure 6g, O^+ number fluxes versus SZA included the upward (Figure 6g, top, with the range from 10^3 to 10^7 cm^{-2} s^{-1}) and downward fluxes (Figure 6g, bottom, with the range from -10^7 to -10^3 cm^{-2} s^{-1}) and triangles represent the averages from both upward and downward fluxes at 5° intervals in SZA. It is interesting to note that the H^+ (Figure 6a) and O^+ densities (Figure 6b) and O^+ number fluxes (Figure 6g) decrease dramatically with increasing SZA in the range 90° to 105°. The straight lines in Figure 6a and Figure 6b are the linear least squares fits for ion densities in log scale. The high correlation coefficients with SZA, $r = 0.93$ for H^+ density and $r = 0.95$ for O^+ density, may suggest that the polar wind is strongly controlled by the solar illumination of the base ionosphere. When the ion density was lower than 0.1 cm^{-3} at perigee (typically the case for H^+ at SZA > 100°), the polar wind signature was seen neither in the chromograms nor in the phase space density velocity distributions, because densities were very low or because the energies were lower than the spacecraft potential (3–5 V at those cases) or for both reasons. Therefore we do not include data in which the density estimate was less than 0.1 cm^{-3} in our study of polar wind characteristics. That is why the H^+ velocity and number flux profiles are not displayed beyond 100° SZA in Figures 6c and 6f. The negative (downward) O^+ velocities and O^+ number fluxes are seen in Figure 6d and 6g for low and high SZA, in general. The O^+/H^+ density ratios (Figure 6e) increase with increasing SZA, but, again, there is an uncertainty for H^+ parameters when the SZA is greater than 100°. We do not include the polar wind perigee data after April 1996 in our survey, because the spacecraft potential was usually higher than 3 V at POLAR perigee. Hence only the O^+ ion distribution was observed after April 1996 at POLAR perigee.

3.2. General Bulk Parameter Trends and Averages for the 5000 km Polar Wind

The polar wind as observed by POLAR/TIDE at 5000 km altitude has several distinguishing characteristics. Occur-
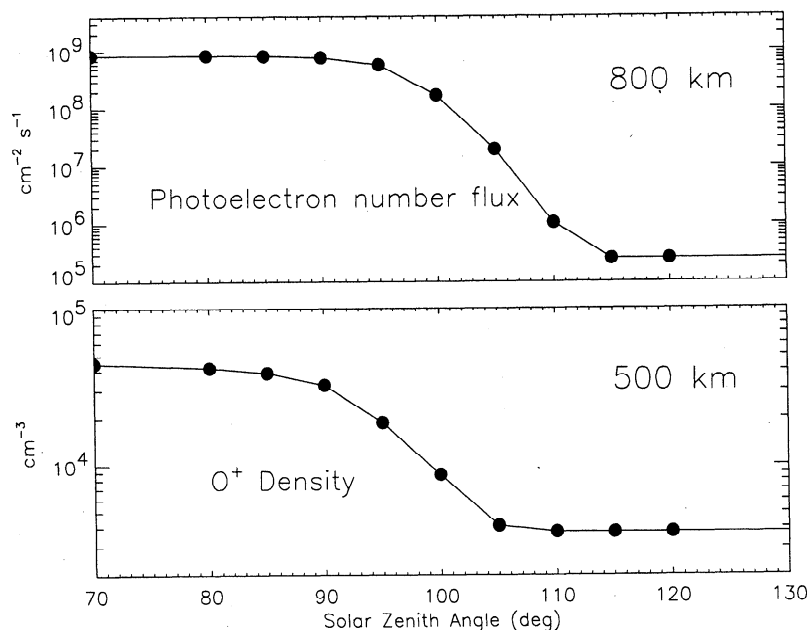
Figure 5. (top) Photoelectron number flux at 800 km altitude and (bottom) O^+ density at 500 km altitude versus solar zenith angle (SZA) from the coupled fluid-semikinetic model [*Su et al.*, 1998].
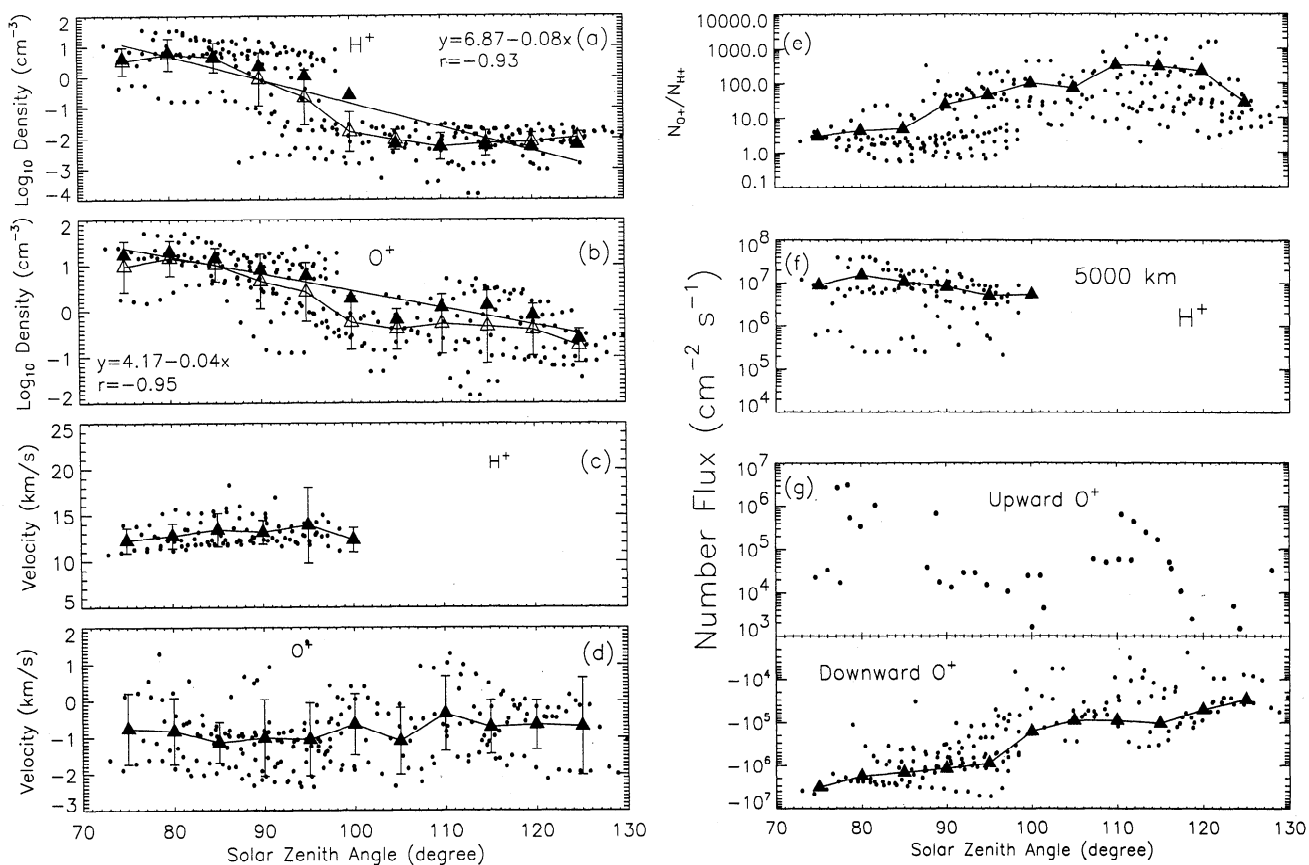

Figure 6. The H^+ and O^+ bulk parameters, including (a) H^+ and (b) O^+ densities in log scale, (c) H^+ and (d) O^+ bulk velocities, (e) O^+/H^+ density ratios, and (f) H^+ and (g) O^+ number fluxes, versus the solar zenith angle. The solid triangles are the linearly averaged values, the open triangles are the logarithmically averaged densities at 5° intervals in SZA. The vertical bar is the standard deviation in log scale in Figures 6a and 6b, and in the linear scale in Figures 6c and 6d. The solid triangles are the average values including both downward (Figure 6g, bottom) and upward fluxes (Figure 6g, top) for O^+ in Figure 6g at 5° intervals in SZA. The straight lines in Figures 6a and 6b are the linear least squares fits in log scale from the average density values. The correlation coefficients r with SZA are 0.93 for the H^+ density and 0.95 for the O^+ density.
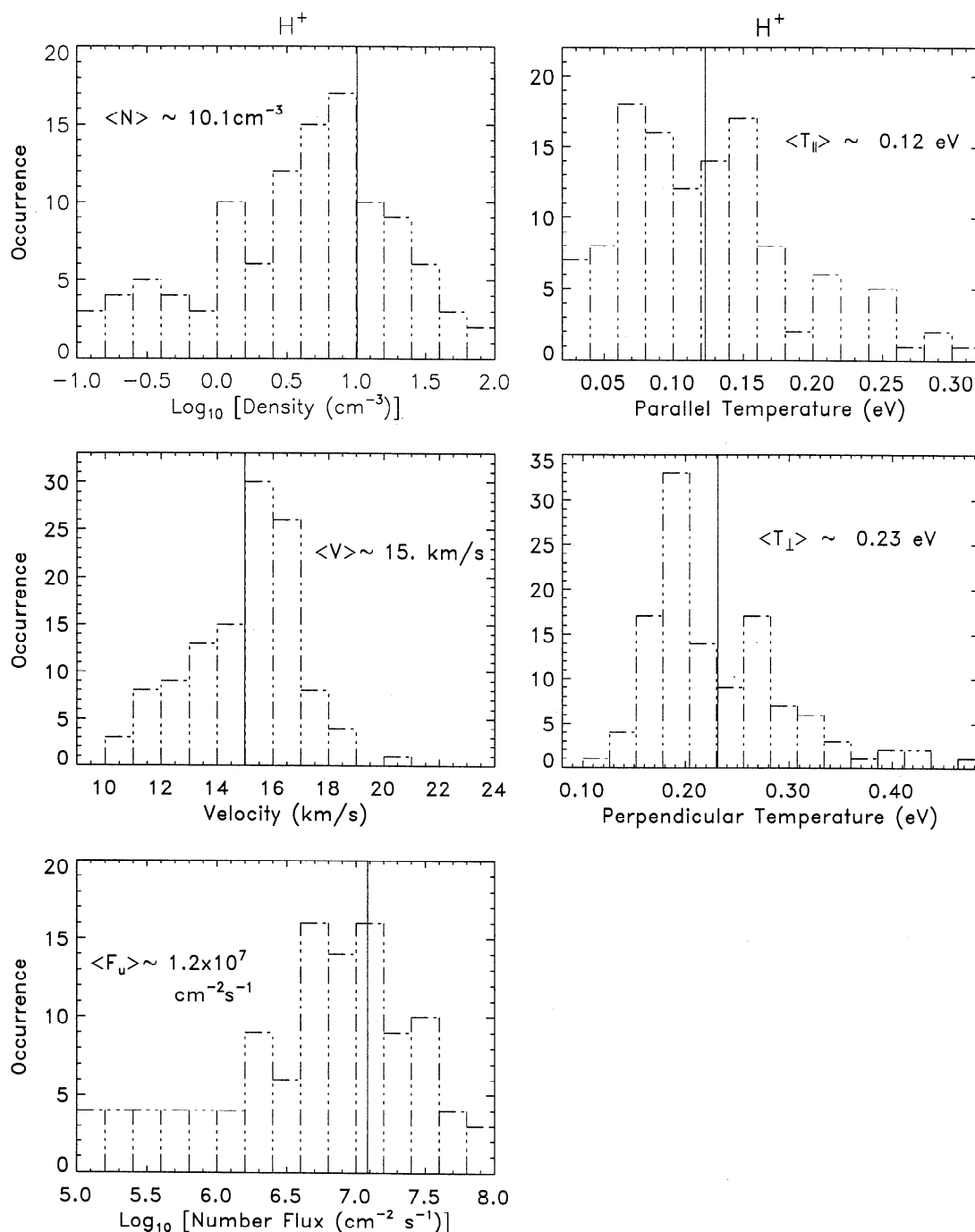
Figure 7. Occurrence frequency histograms for the H^+ bulk parameters, including (a) density, (b) parallel temperature, (c) parallel velocity, (d) perpendicular temperature, and (e) parallel number flux at 5000 km altitude. The vertical solid lines represent the average values.

rence histograms for H^+ bulk parameters are shown in Figure 7, including density (Figure 7a), parallel velocity (Figure 7c), parallel number flux (Figure 7e), parallel temperature (Figure 7b), and perpendicular temperature histograms (Figure 7d). Most of the data were sampled for the lower SZA ($\leq 100°$) regions when the H^+ density was greater than our threshold density, 0.1 cm^{-3}. The H^+ densities at 5000 km range from 0.1 to 100 cm^{-3}, the H^+ parallel velocities range from 10 to 21 km s^{-1}, the H^+ parallel number fluxes range from 10^5 to 10^8 cm^{-2} s^{-1}, and the parallel and perpendicular temperatures range from

0.05 to 0.45 eV. The average H^+ density, parallel velocity, number flux, parallel temperature, and perpendicular temperature are ~10 cm^{-3}, 15 km s^{-1}, 1.2×10^7 cm^{-2} s^{-1}, 0.12 eV (~1390 K), and 0.23 eV (~2670 K), respectively.

Occurrence plots for O^+ bulk parameters are shown in Figure 8, including density (Figure 8a), parallel velocity (Figure 8c), parallel downward (Figure 8e) and upward number flux (Figure 8f), parallel temperature (Figure 8b), and perpendicular temperature histograms (Figure 8d). The lines with solid circles are summed from a total of 20 POLAR perigee passes,
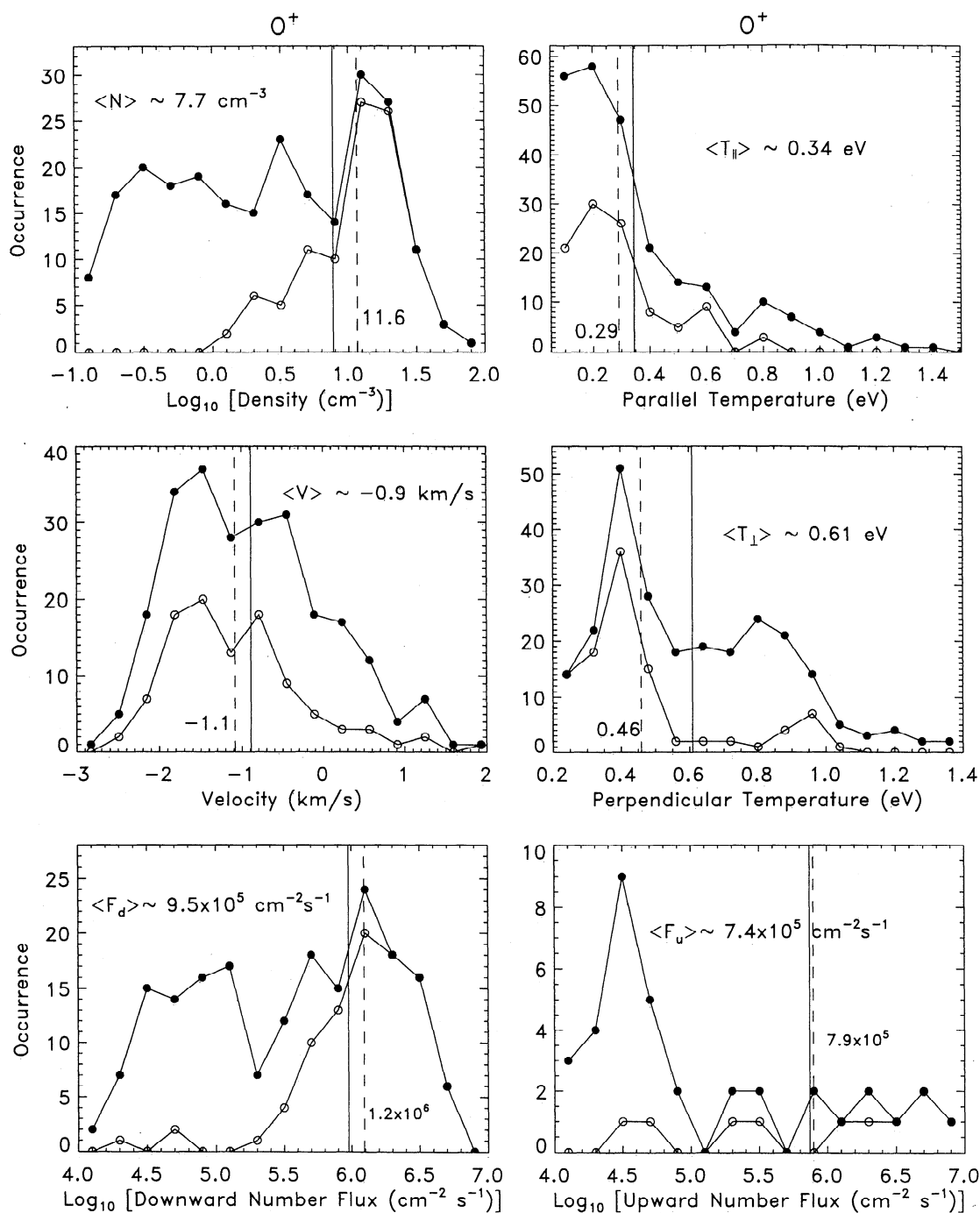
Figure 8. Occurrence frequency histograms for the O^+ bulk parameters, including (a) density, (b) parallel temperature, (c) parallel velocity, (d) perpendicular temperature, and (e) downward and (f) upward number fluxes at 5000 km altitude. The lines with the solid circles are the occurrence frequencies based on 20 perigee passes, with the average values shown as the vertical solid lines. The lines with the open circles are the occurrence summed from the data at the low solar zenith angle (SZA < 110°) region only, with the average values shown as vertical dashed lines.

with the average value displayed by the vertical solid line. The lines with open circles are for the low SZA ($\leq 100°$) passes only, with the average shown as the vertical dashed line. The O^+ densities range from 0.1 to 100 cm^{-3}, the velocities range from -3 to 2 km s^{-1}, the downward and upward parallel number fluxes range from 10^4 to 10^7 cm^{-2} s^{-1}, and the parallel and perpendicular temperatures range from 0.2 to 1.4 eV. We have observed mostly downward O^+ flows at 5000 km altitude

in the polar cap, which is consistent with the DE 1 observations in the polar cap by *Chandler* [1995]. This may provide additional confirmation of the results of cleft ion fountain analyses [*Lockwood et al.,* 1985a, b; *Horwitz and Lockwood,* 1985; *Horwitz,* 1987]. The average O^+ density, bulk velocity, parallel temperature, perpendicular temperature, downward number flux, and upward number flux for total of 20 perigee passes (lower SZA regions only) are 7.7 (11.6) cm^{-3}, -0.9
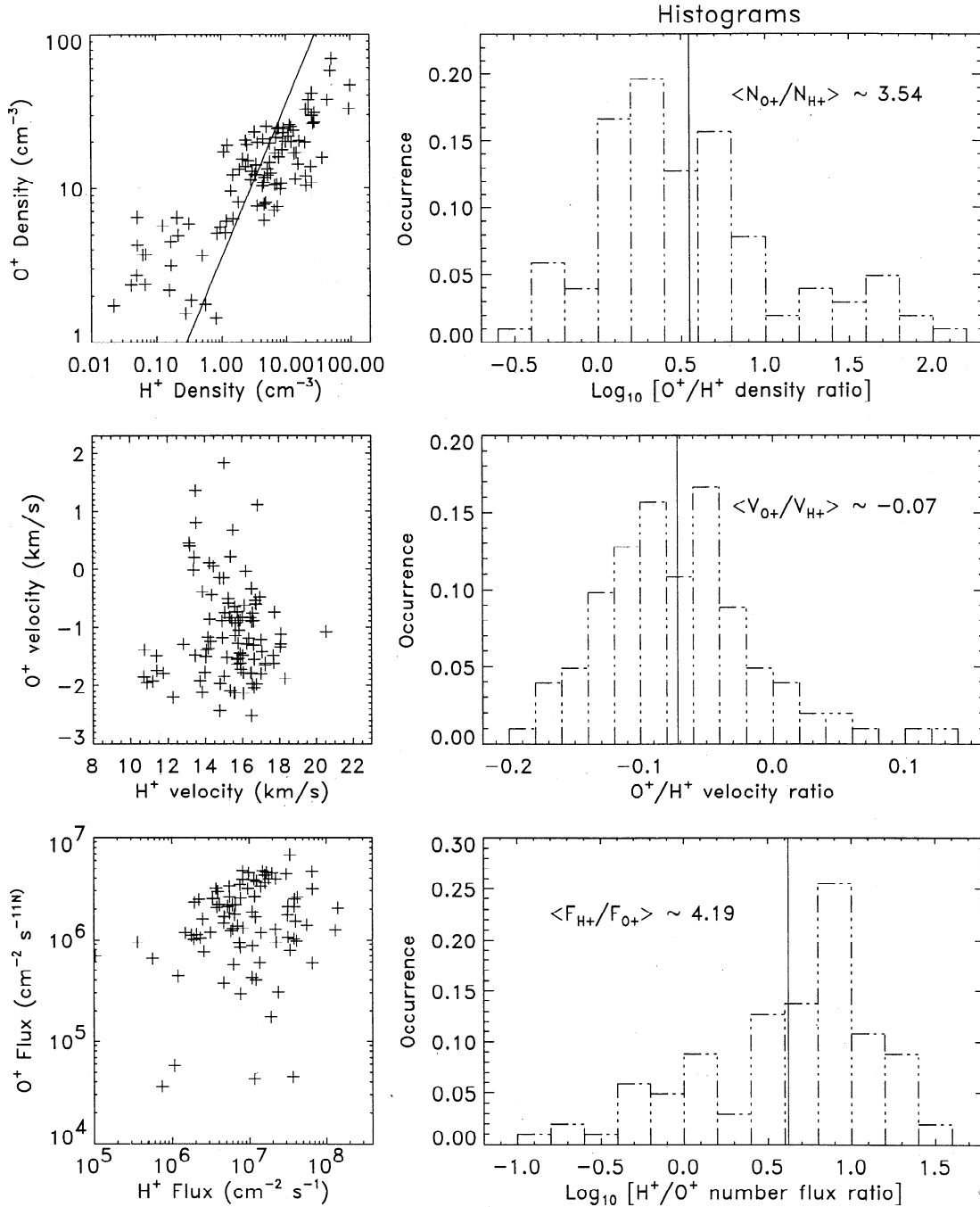
Figure 9. (right) Occurrence frequency histograms for the (top) O^+/H^+ density ratios, (middle) parallel velocity ratios, and (bottom) the absolute number flux. The density and number flux ratio histograms are in log scale. (left) O^+ versus H^+ bulk parameters, including (top) densities, (middle) bulk velocities, and (bottom) absolute density fluxes, with solid lines representing the average values.

(−1.1) km s^{-1}, 0.34 (0.29) eV, 0.61 (0.46) eV, 9.5 × 10^5 (1.2 × 10^6) cm^{-2} s^{-1}, and 7.4 × 10^5 (7.9 × 10^5) cm^{-2} s^{-1}, respectively.

We are also interested in the O^+/H^+ ratios for the various bulk parameters. Plots of O^+ versus H^+ in density, parallel velocity, and absolute number flux are shown in Figure 9 (left) and the O^+/H^+ density and parallel velocity ratio and absolute H^+/O^+ number flux ratio histograms are displayed in Figure 9 (right), where the solid lines represent the average ratios. In Figure 9, both H^+ and O^+ data are from low SZA regions only. The O^+/H^+ average density ratio is ~ 3.5, so O^+ is the dominant

ion species at 5000 km altitude. The average H^+/O^+ absolute flux ratio is ~ 4.2, since H^+ ions have much higher velocities than O^+ ions. The O^+ velocities are primarily negative (downward) in our survey.

Plots of the perpendicular versus parallel temperatures for H^+ and O^+ are shown in Figure 10 (left) and the parallel/perpendicular temperature ratio histograms for H^+ and O^+ are shown in Figure 10 (right), where the solid lines represent the average ratios. The average parallel/perpendicular temperature ratios are 0.46 for H^+ ions and 0.58 for O^+ ions. The per-
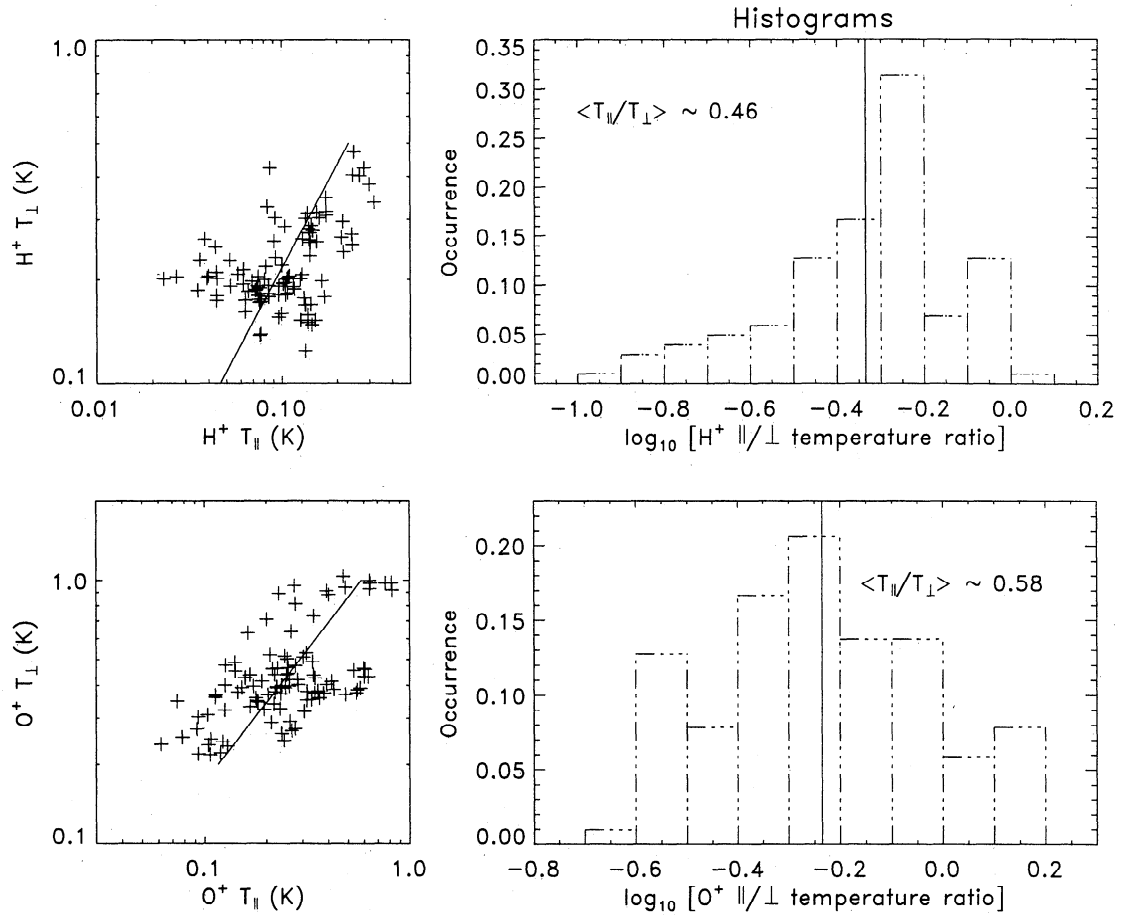
Figure 10. (right) Occurrence frequency histograms for the parallel/perpendicular temperature ratios for (top) H^+ and (bottom) O^+ in log scale. (left) Parallel temperature versus perpendicular temperature for (top) H^+ and (bottom) O^+, with solid lines representing the average values.

pendicular temperatures tend to be about twice the parallel temperatures for both H^+ and O^+ ions ($T_{\perp i} \sim 2T_{\parallel i}$), which may suggest perpendicular ion heating at or below 5000 km altitude.

Plots of the O^+ versus H^+ temperatures are shown in Figure 11 (left) and the ratio histograms are shown in Figure 11 (right), with parallel temperatures at top and perpendicular temperatures at bottom. The solid lines represent the average temperature ratios. The O^+ parallel temperature is, on average, 2.5 times higher than the H^+ parallel temperature, and the O^+ perpendicular temperature is about twice that of H^+, consistent with O^+ ions having generally higher energies than H^+ ions. This may be due, in part, to cleft ion fountain heating of O^+.

H^+ (top) and O^+ (bottom) parallel Mach number histograms are shown in Figure 12, where the solid lines represent the average values. The H^+ Mach numbers range from 2.2 to 5, with an average of 3.7, which indicates that H^+ supersonic outflow exhibited at 5000 km altitude. The average O^+ Mach number is about −0.7, indicating, again, O^+ subsonic downflow, in general, within the polar cap.

3.3. Relationship With Day-Night Distance in Solar Magnetic Coordinate System

The cleft ion fountain paradigm for O^+ would predict that the ion densities, parallel velocities, and parallel temperatures

decrease from dayside to nightside [e.g., *Horwitz and Lockwood*, 1985; *Horwitz et al.*, 1985]. An examination of the TIDE polar wind data versus the Sun-Earth axis in the solar magnetic coordinate system (X_{SM}) was performed to investigate this suggestion. In the solar magnetic coordinate system, the z axis is chosen parallel to the north magnetic pole, the y axis is perpendicular to the Earth-Sun line toward dusk, and the x axis is in the other plane, positive toward the Sun. Plotting the data versus X_{SM} is equivalent to mapping the data to the noon-midnight plane of the polar magnetosphere. The H^+ ion densities, O^+ ion densities, O^+ parallel velocities, O^+ downward number fluxes, and O^+ parallel temperatures versus X_{SM} are shown in Figures 13a–13e, respectively. The solid lines in the H^+ and O^+ density plots are the linear least squares fits, using the logarithmically averaged densities at 0.11 R_E intervals in X_{SM}. Figure 13b shows a very strong linear decline of O^+ densities with X_{SM}, with a high correlation coefficient, $r = 0.98$. The H^+ density correlation coefficient is 0.93 in Figure 13a, but, again, there is an uncertainty when the densities were less than 0.1 cm^{-3}. The O^+ densities and number fluxes increase from the nightside to the dayside, which would indicate a cleft ion fountain origin [*Lockwood et al.*, 1985a,b; *Horwitz and Lockwood*, 1985], but the trends for the parallel velocities and parallel temperatures with X_{SM} are not conclusive.
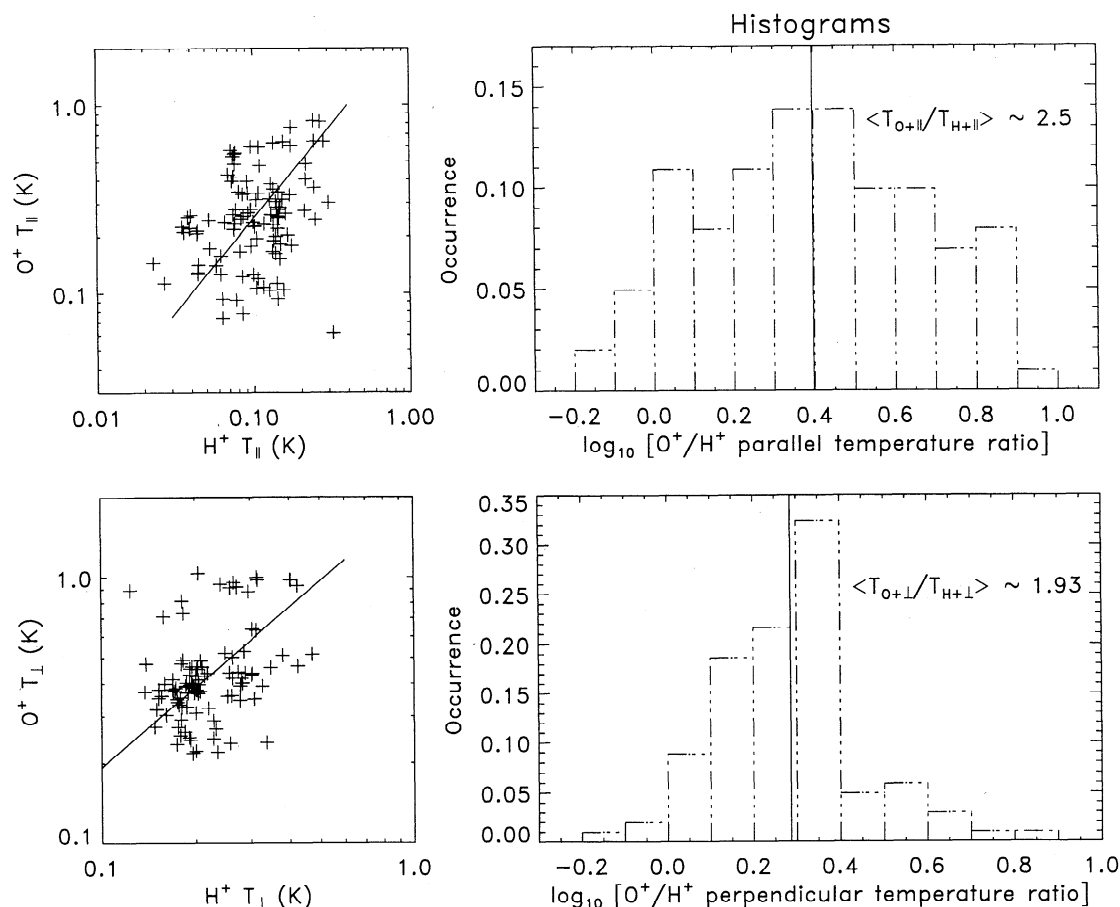
Histograms

Figure 11. (right) Occurrence frequency histograms for the O^+/H^+ (top) parallel and (bottom) perpendicular temperature ratios in log scale. (left) O^+ versus H^+ temperature for (top) parallel and (bottom) perpendicular components, with solid lines representing the average values.

4. Survey of 8 R_E Altitude Polar Wind With PSI Operation

When the POLAR satellite was near apogee in the northern hemisphere during 1996, the spacecraft typically attained large positive electric potentials of 40 V or more owing to the very low plasma densities in the high-altitude polar cap as well as the photoelectron emission from the spacecraft. The Plasma Source Instrument [*Moore et al.,* 1995] is a xenon plasma source, whose associated electrons balance the photoelectron escape current and whose low electron temperature regulates the spacecraft potential to low values. The POLAR floating potential is monitored by the electric field instrument (EFI) [*Harvey et al.,* 1995] on POLAR, using three pairs of multielement probes. Measurement of the resultant potential by EFI shows that the potential is stabilized at about +1.8–2.2 V, when PSI was turned on, allowing TIDE measurements of low-energy ions in regions of very low plasma density [cf. *Moore et al.,* 1997; *Comfort et al.,* 1998]. In order to observe this high-altitude polar wind outflow, PSI operation is necessary. Unfortunately, our polar wind survey at high altitude included only limited polar wind data at apogee from TIDE with PSI operating during the early portion of the POLAR mission. In this paper we focus on three long POLAR apogee passes in April and May 1996. In summer

1996, TIDE lost its mass analysis capability. Since then, a considerable volume of polar wind data has been obtained with PSI running, but mass separation is not routinely possible and new analysis techniques will have to be developed for that data, which will be the subject of future studies.

Typical O^+ and H^+ ion distributions from 1743:44 to 1744:43 UT (1 min average) on April 19, 1996, are shown in Figures 14a and 14b. Since the apogee of the POLAR orbit was in the northern hemisphere, the negative x is in the direction along the magnetic field line away from Earth. In Figure 14a (left), the phase space density distribution is sliced in the y-z plane perpendicular to the local magnetic field for an O^+ velocity of $V_x = -28.5$ km s^{-1}. Figure 14a (right) shows a slice in the parallel x-y plane with $V_z = -4.1$ km s^{-1}. Likewise, a perpendicular plane of H^+ distribution with $V_x = -47.7$ km s^{-1} is seen in Figure 14b (left), while Figure 14b (right) shows a parallel plane with $V_z = -4.8$ km s^{-1}. Both ion species were observed to be flowing out of the northern polar cap with high parallel velocities along the magnetic field lines. The spacecraft potential in this case was 1.94 V when PSI was operating. The O^+ and H^+ ion energies at apogee tend to be sufficient such that ion distributions were not significantly shielded by this residual 1.94 V spacecraft potential. The Poisson statistics error estimations associated with the individual measurements as discussed at the end of section 2 for this typical

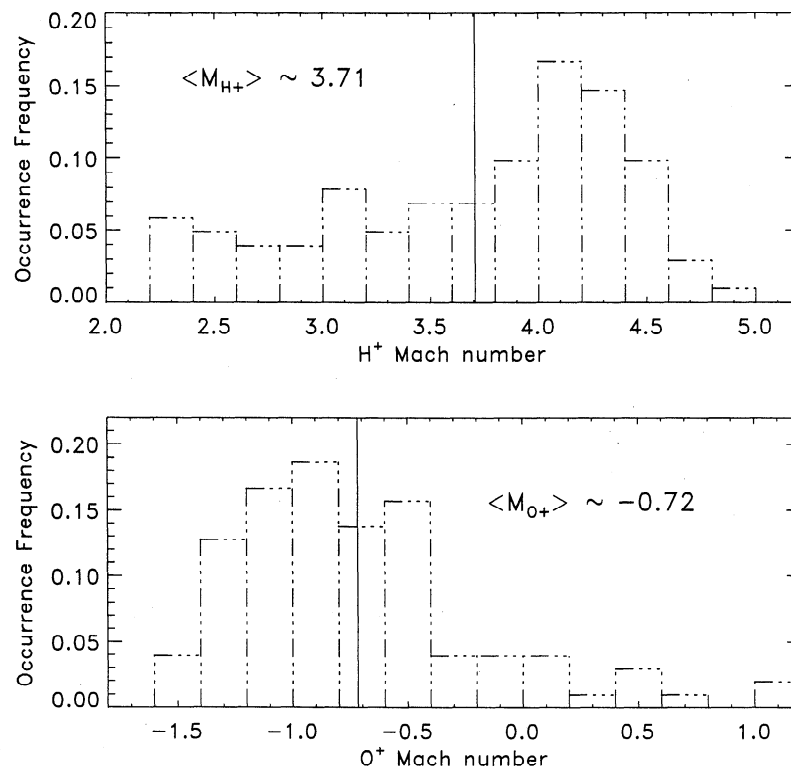## Mach number histograms at 5000 km altitude

Figure 12. Mach numbers histograms for polar cap (top) H^+ and (bottom) O^+ at 5000 km altitude, with solid lines representing the average Mach numbers.

POLAR apogee case in Figures 14a and 14b are ~ 2.65% for H^+ (1426 counts per sample) and ~ 8% for O^+ (156 counts per sample). However, other sources of errors may be larger.

In this section, we present polar wind characteristics and general trends in bulk parameters at POLAR apogee. We then discuss the relationship of parameters with day-night distance in the solar magnetic (SM) coordinate system at 8 R_E altitude. Each sample data here is averaged over 1 min.

4.1. General Bulk Parameter Trends and Averages for the 8 R_E Polar Wind

The newly discovered polar wind from POLAR TIDE PSI at 8 R_E altitude has several distinguishing characteristics, which are shown in Figures 15–22, including densities, parallel velocities, number fluxes, and parallel and perpendicular temperatures for three ion species, H^+, O^+, and He^+. We should note that the parameter estimates for He^+ in this paper are somewhat uncertain, since the He^+ data from TIDE were generally very close to the instrument noise level.

Occurrence frequency histograms for the H^+ polar wind parameters at 8 R_E altitude are shown in Figure 15, including density (Figure 15a), parallel velocity (Figure 15c), parallel number flux (Figure 15e), and parallel and perpendicular temperatures (Figures 15b and 15d), where the solid lines represent the average values. The H^+ densities range from 0.01 to 2 cm^{-3}, with an average value of ~0.3 cm^{-3}, while the H^+ parallel velocities range from 20 to 110 km s^{-1}, with and average of 45 km s^{-1}. All H^+ ions flow away from the Earth along magnetic

field lines with a broad bulk flow velocity range. The H^+ outflow is a long-duration outflow which lasted for several hours at high altitudes over the polar cap. The H^+ parallel number flux was of order 10^5–10^7 cm^{-2} s^{-1}, with an average 1.2×10^6 cm^{-2} s^{-1}. The average parallel and perpendicular temperatures for H^+ at high altitudes were ~ 1.7 and 1.1 eV, ranging from 0.1 to 10 eV.

The corresponding occurrence frequency histograms for the O^+ polar wind parameters are shown in Figure 16, where the solid lines represent the average values again. The O^+ density was in the range 1×10^{-3}–0.3 cm^{-3}, with an average of 0.05 cm^{-3}, and the O^+ parallel velocity ranged between 8 and 32 km s^{-1}, with an average of ~ 17 km s^{-1}. At these high altitudes, all O^+ ions flow away from the Earth along the field lines. The O^+ parallel upward number flux ranged between 10^3 and 10^6 cm^{-2} s^{-1}, with an average of 8.3×10^4 cm^{-2} s^{-1}. The average O^+ parallel and perpendicular temperatures were ~ 7.5 and 3.4 eV, both temperatures ranging from 0.2 to 30 eV.

The He^+ counts near apogee were often low and close to the instrument noise level and thus, at times, provided unreliable bulk parameter estimates from the analysis procedure, in particular, very low He^+ parallel and perpendicular temperatures (from 10^{-1} to 10^{-3} eV) for a number of He^+ samples. TIDE counts respond to ion energy flux, and we found that when we examined the parallel and perpendicular temperatures versus He^+ energy density ($N \times T$), that the evidently spurious temperatures occurred only for He^+ energy densities below 10^{-3} eV cm^{-3} (using either parallel or perpendicular temperatures). Therefore, for the He^+ results in this paper, in Figures 17–20, we
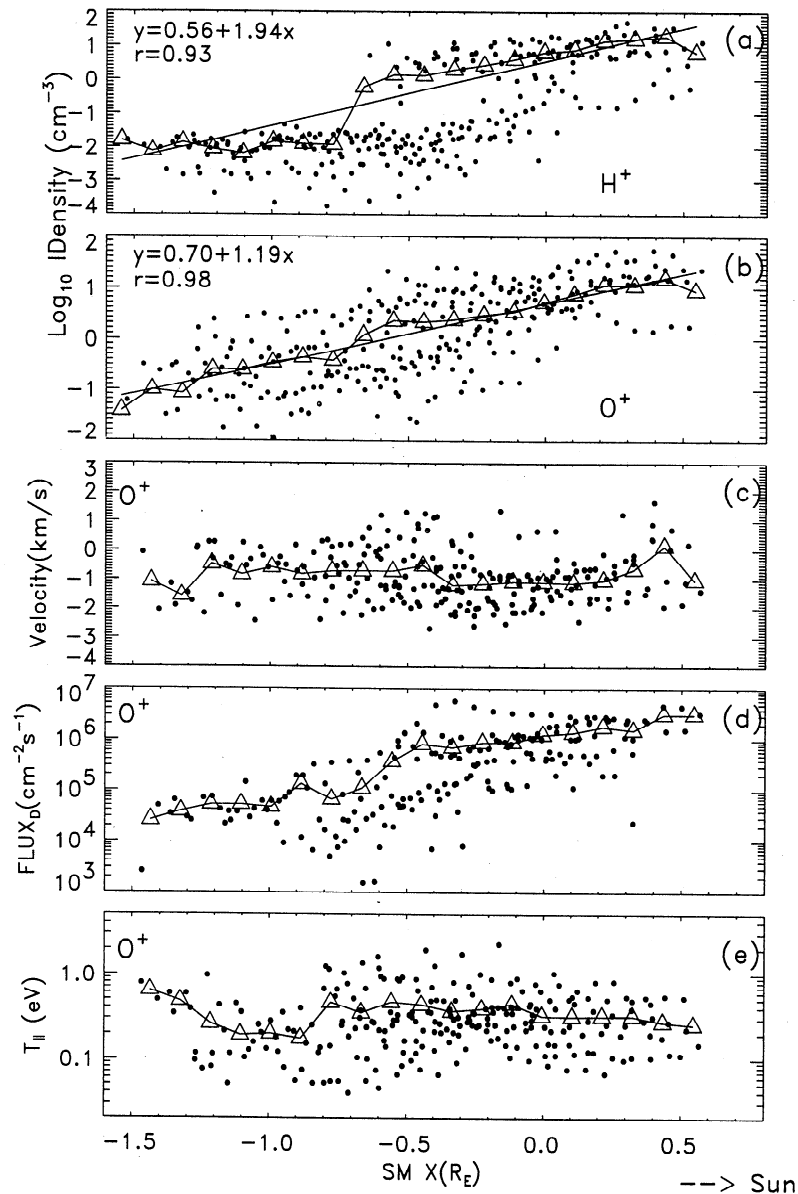
Figure 13. The bulk parameters, including (a) H^+ densities, (b) O^+ densities, (c) O^+ velocities, (d) O^+ downward fluxes, and (e) O^+ parallel temperatures versus X_{SM}. The open triangles with solid lines are the values averaged over the interval of 0.11 R_E in X_{SM}. The straight lines in Figures 13a and 13b are the linear least squares fits in the log scale from the average density points. The correlation coefficients are 0.93 for the H^+ densities and 0.98 for the O^+ densities.

have only included He^+ bulk parameters for samples in which the parallel and perpendicular He^+ energy densities exceeded 10^{-3} eV cm^{-3}.

The He^+ density (Figure 17a), parallel velocity (Figure 17c), number flux (Figure 17e), and parallel and perpendicular temperature (Figures 17b and 17d) histograms are shown in Figure 17. The He^+ density was in the range 10^{-3}–0.1 cm^{-3}, with an average of 0.012 cm^{-3}, and the parallel velocity ranged

between 8 and 63 km s^{-1}, with an average upward velocity of ~ 25.4 km s^{-1}. The He^+ parallel number flux was in the range 10^3–10^5 cm^{-2} s^{-1}, with an average of 2.5 × 10^4 cm^{-2} s^{-1}. The average parallel and perpendicular temperatures for He^+ were ~ 3.0 and 1.5 eV, respectively. The He^+ peak counts per sample (1 min sample) was less than 25 counts, so the Poisson statistics uncertainty percentages are estimated to be larger than 20%.

In addition to the high-altitude polar wind characteristics,

Figure 14a. The typical phase space density velocity distribution for O^+ at apogee from 1743:44 to 1744:43 UT on April 19, 1996. The coordinate system is defined as in Figure 1. The phase-spaced density distribution is sliced (left) in the plane perpendicular to the local magnetic field for an velocity of V_X = −28.5 km s^{-1}. (right) Slice in the parallel plane with V_Z = −4.1 km s^{-1}. Here the negative V_x means the polar wind is flowing outward from the Earth along the magnetic field lines in the northern hemisphere. The spacecraft potential is 1.94 V in this case. *(opposite)*

TIDE Phase Space Density Velocity Distribution Plots
04/19/96 17:43:44 to 17:44:43 UT

mag_el: 91°

mag_az: 292°

s/c pot: 1.94   0.02 v

gse_dec: 0.42 rad

gse_r_asc: 4.69 rad

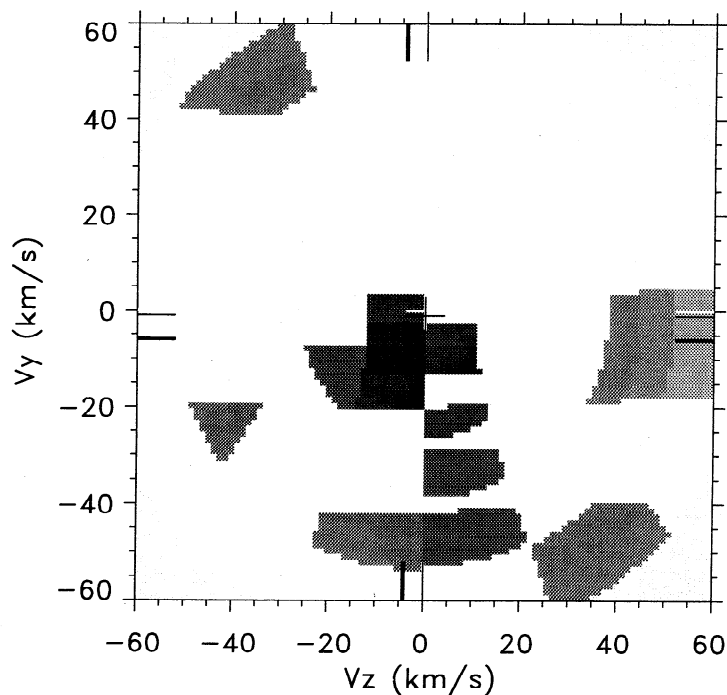Re: 8.2297

Lshell: 100.000

mlt: 23.5 hr

mlat: 77.878°

invlat: 85.796°

TIDE on, PSI on

Vsc-X:-1.62e+00 km/s

Vsc-Y:-9.78e-01 km/s

Vsc-Z:-1.12e-02 km/s

moments calculation ranges:
energy (RPA V): 0.00- 85.00
spin angle:112.50-202.50°
polar channels: 3-6

den: 4.96e-02 cm^{-3}

t_parl: 1.03e+01 eV

t_perp: 3.55e+00 eV

Vpl-X:-2.85e+01 km/s

Vpl-Y:-6.01e+00 km/s

Vpl-Z:-4.11e+00 km/s

earth

+ spacecraft

+ plasma

$O+$

Perpendicular Plane
Vx = -28.5 km/s

Parallel Plane
Vz = -4.1 km/s
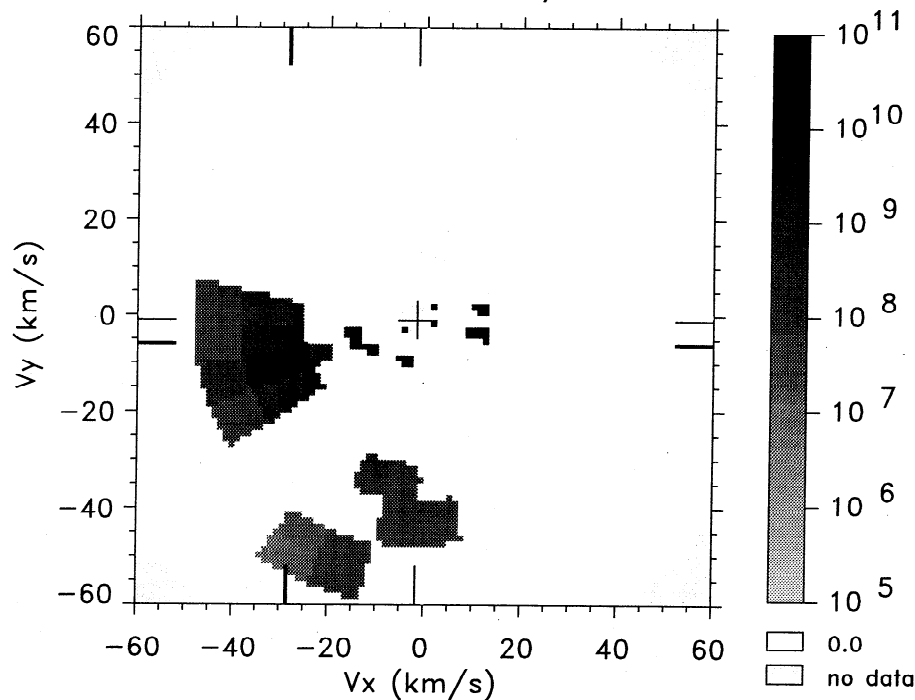
SEC^3 KM^{-6}

10^{11}

10^{10}

10^9

10^8

10^7

10^6

10^5

0.0

no data

TIDE Phase Space Density Velocity Distribution Plots
04/19/96 17:43:44 to 17:44:43 UT

mag_el: 91°

mag_az: 292°

s/c pot: 1.94   0.02 v

gse_dec: 0.42 rad

gse_r_asc: 4.69 rad

Re: 8.2297

Lshell: 100.000

mlt: 23.5 hr

mlat: 77.878°

invlat: 85.796°

TIDE on, PSI on

Vsc-X:-1.62e+00 km/s

Vsc-Y:-9.78e-01 km/s

Vsc-Z:-1.12e-02 km/s

moments calculation ranges:
energy (RPA V): 0.00- 40.00
spin angle:112.50-202.50°
polar channels: 3-6

den: 3.36e-01 cm^{-3}

t_parl: 1.24e+00 eV

t_perp: 8.26e-01 eV

Vpl-X:-4.77e+01 km/s

Vpl-Y:-6.56e+00 km/s

Vpl-Z:-4.77e+00 km/s

earth
+ spacecraft
+ plasma

H+

Perpendicular Plane
Vx = -47.7 km/s

Parallel Plane
Vz = -4.8 km/s

SEC^3 KM^{-6}
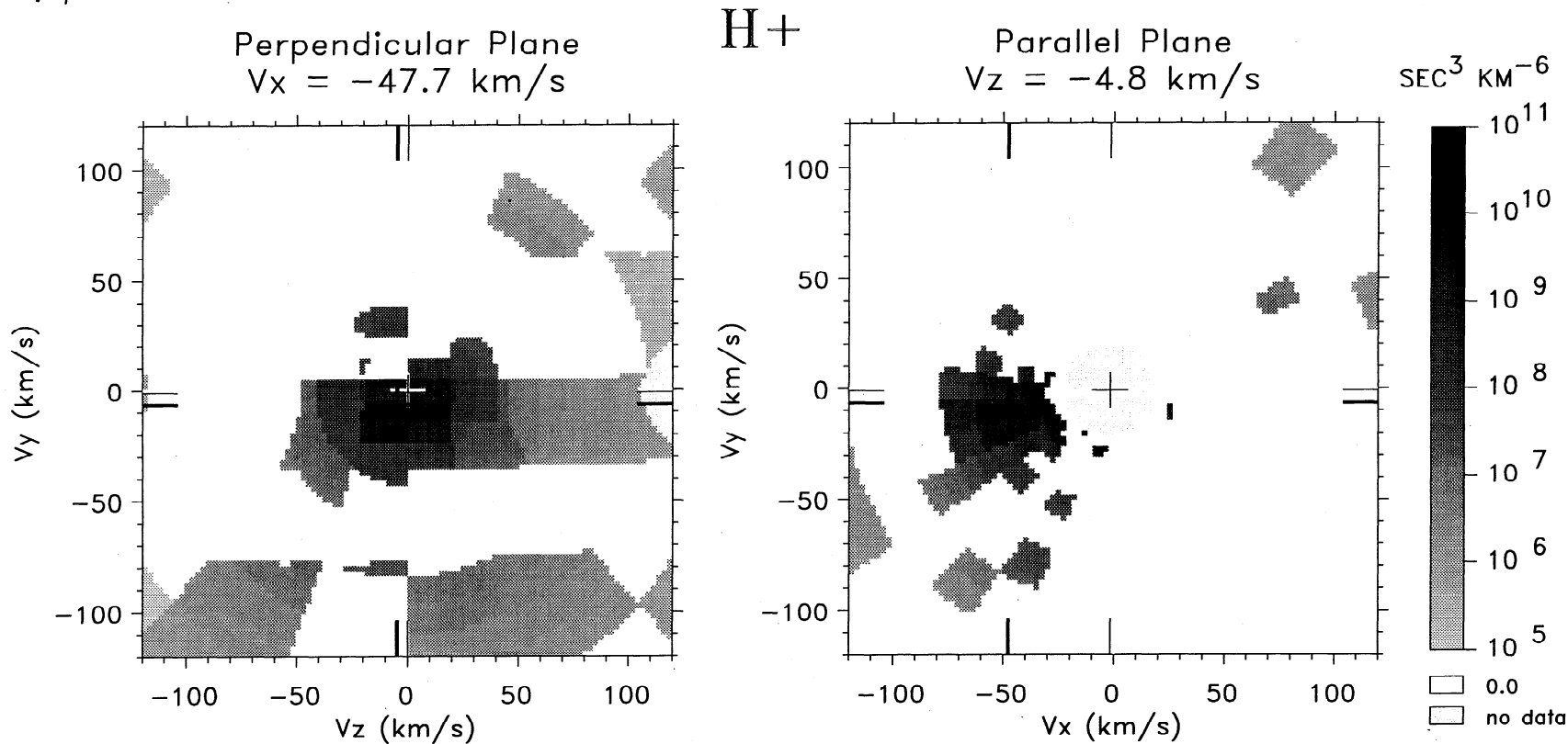
Figure 14b. Same as Figure 14a, but for H$^+$, (left) a perpendicular plane of H$^+$ distribution with $V_X = -47.4$ km s^{-1} and (right) a parallel plane with $V_Z = -4.8$ km s^{-1}. Note that the velocity scales differ between Figures 14a and 14b.
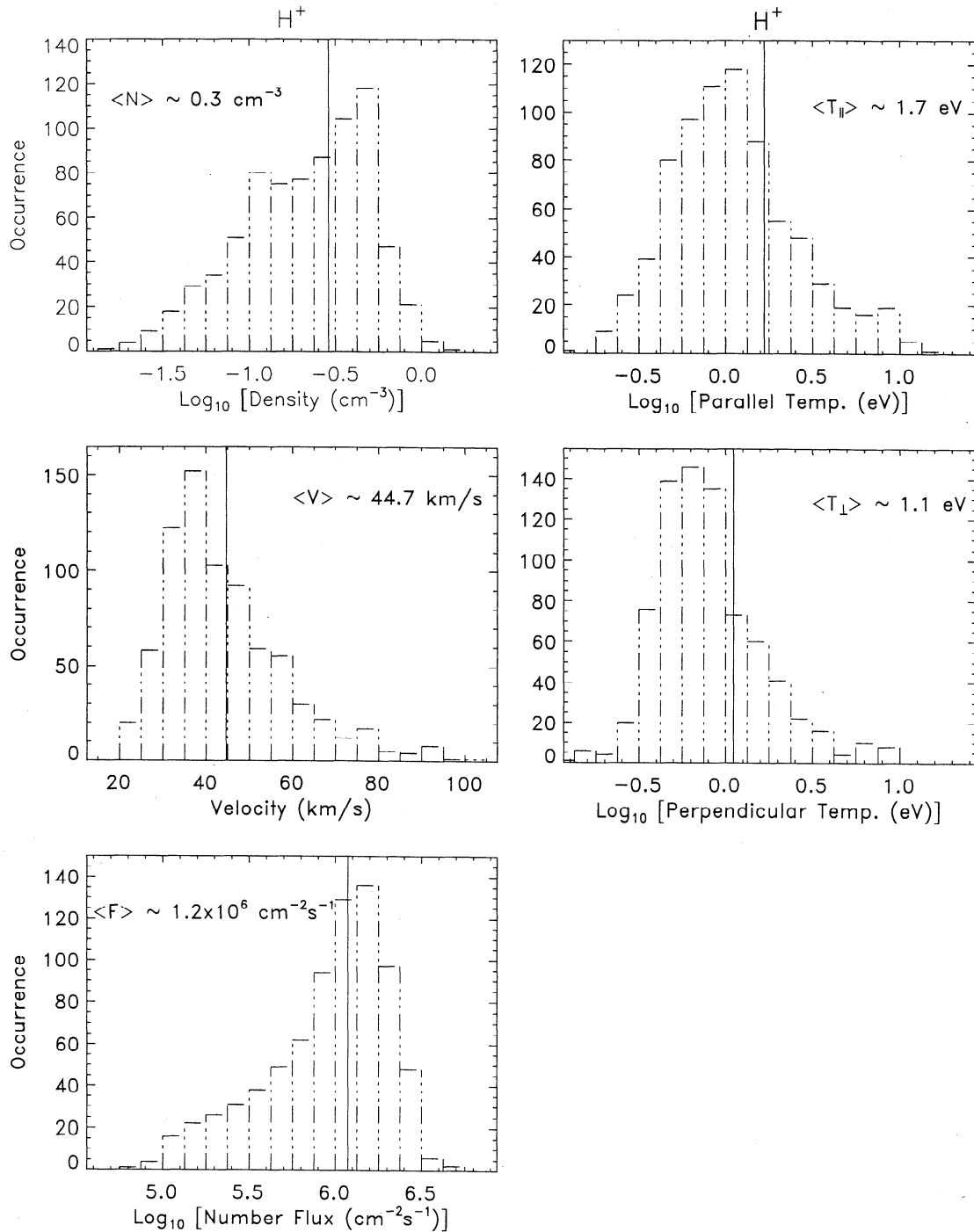
Figure 15. Histograms for H$^+$ bulk parameters, including (a) densities, (b) parallel temperatures, (c) parallel velocities, (d) perpendicular temperatures, and (e) number fluxes at 8 R_E altitude, with vertical solid lines representing the average values.

we are also interested in the ratios of bulk parameters for these three ion species. The occurrence frequency histograms of density ratios for H$^+$, O$^+$, and He$^+$ are presented in log scale in Figure 18 (right), including O$^+$/H$^+$ (top), He$^+$/O$^+$ (middle), and He$^+$/H$^+$ (bottom) density ratios, where the solid lines represent the average density ratios. Plots of O$^+$ versus H$^+$ densities (top), He$^+$ versus O$^+$ densities (middle), and He$^+$ versus H$^+$ densities (bottom) are shown in Figure 18 (left). The average O$^+$/H$^+$ density ratio was 0.16, while the average He$^+$/O$^+$ and

He$^+$/H$^+$ ratios were 0.18 and 0.03, respectively. Figure 18 indicates that the H$^+$ ions were the highly dominant ion species at high altitudes. The average density ratios for these three ion species were N_{He+} : N_{O+} : N_{H+} ~ 1 : 6 : 38, as summarized from Figure 18.

The occurrence frequency histograms of the velocity ratios for H$^+$, O$^+$, and He$^+$ are presented in Figure 19 (right), including O$^+$/H$^+$ (top), O$^+$/He$^+$ (middle), and He$^+$/H$^+$ (bottom) velocity ratios in linear scale, where the solid lines represent the
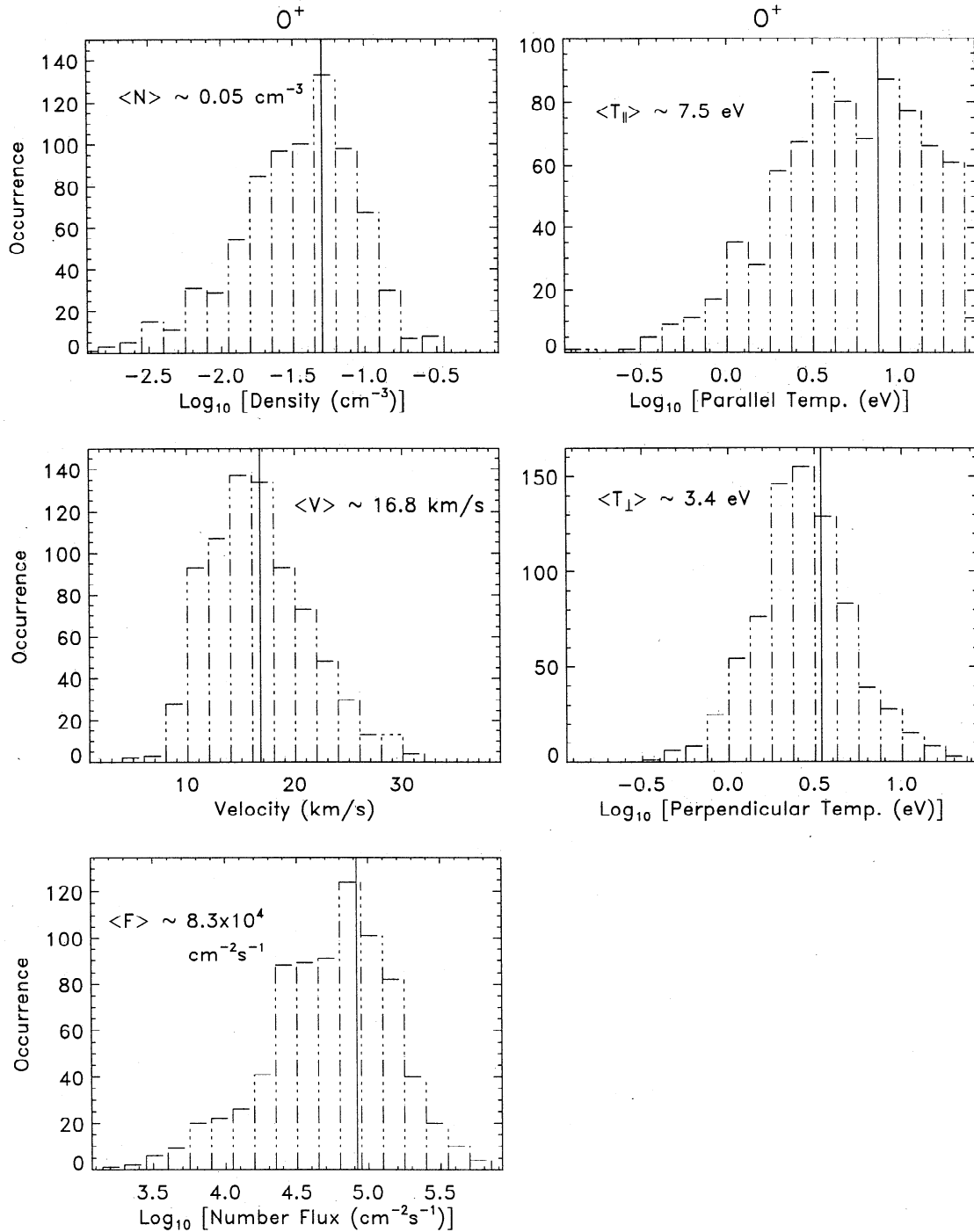
Figure 16. Histograms for O$^+$ bulk parameters, including (a) densities, (b) parallel temperatures, (c) parallel velocities, (d) perpendicular temperatures, and (e) number fluxes at POLAR apogee, with vertical solid lines representing the average values.

average velocity ratios. Plots of O$^+$ versus H$^+$ velocities (top), O$^+$ versus He$^+$ velocities (middle), and He$^+$ versus H$^+$ velocities (bottom) are shown in Figure 19 (left). The dashed lines in Figure 19 represent the equal energy gain ratios, V_{O+} : V_{He+} : V_{H+} = 1 : 2 : 4, which would suggest equal energy gains for all three ions, such as via a photoelectron-driven electrostatic potential layer [*Su et al.*, 1998]. The average O$^+$/H$^+$, O$^+$/He$^+$, and He$^+$/H$^+$ velocity ratios were 0.40, 0.74, and 0.59, respectively. The average parallel velocity ratios for all three ion

species were V_{O+} : V_{He+} : V_{H+} ~ 2 : 3 : 5, as summarized from Figure 19. For velocity ratios near 1, the velocity filter (e.g., from the cleft ion fountain [*Horwitz and Lockwood*, 1985]) and/or centrifugal acceleration effects [*Horwitz et al.*, 1994] may be dominant. The observed ratios span all of these possibilities, so all of these effects, gravitational force, velocity filter, centrifugal acceleration, and electrostatic acceleration, may be involved in the transport of polar wind. However, the "typical" velocity ratios, V_{O+} : V_{He+} : V_{H+} ~ 2 : 3 : 5, are
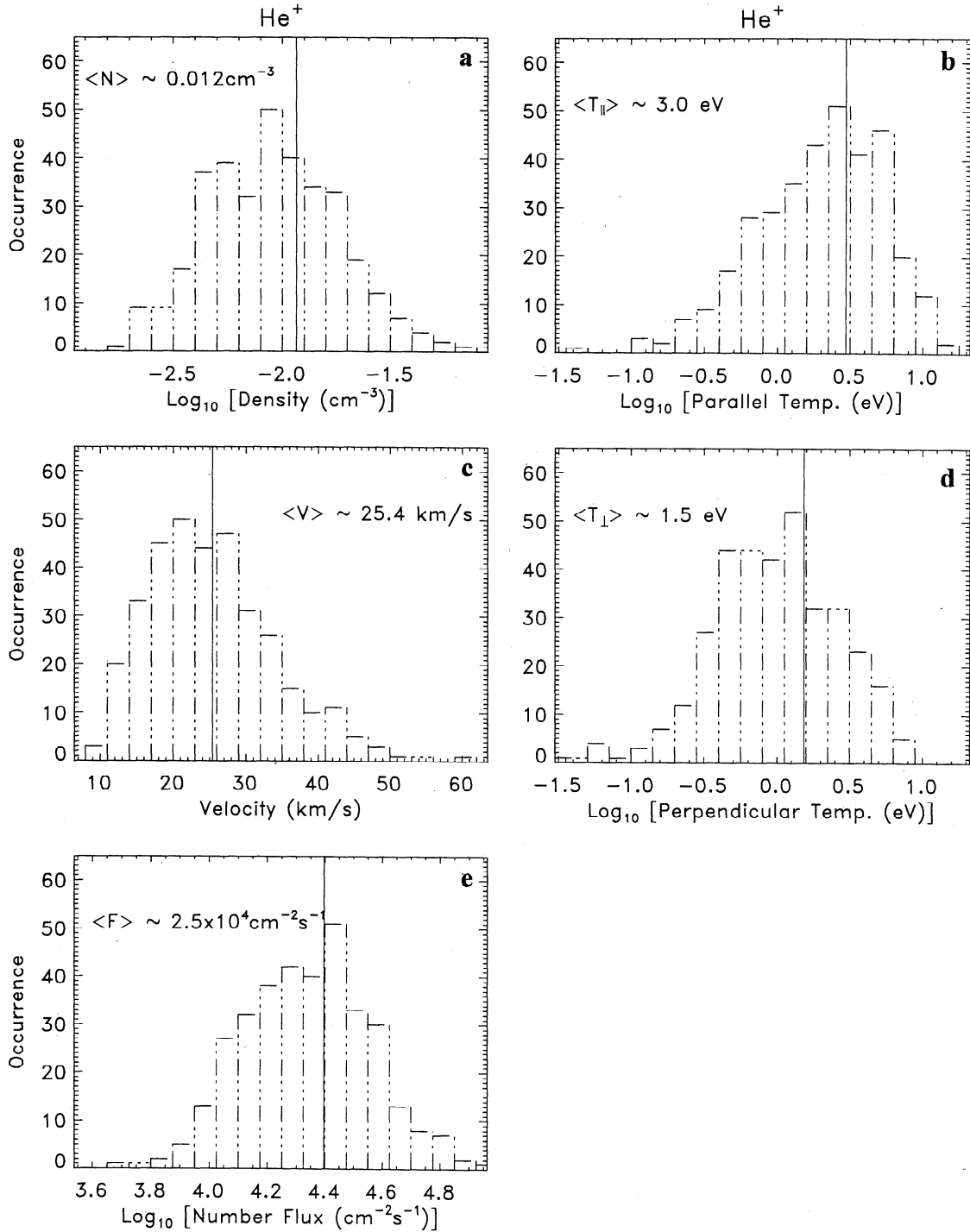
Figure 17. Histograms for He$^+$ bulk parameters, including (a) densities, (b) parallel temperatures, (c) parallel velocities, (d) perpendicular temperatures, and (e) number fluxes at 8 R_E altitude, with vertical solid lines representing the average values.

somewhat more suggestive of the importance of comparable energy gains for the ion species.

The corresponding histograms for H$^+$, O$^+$, and He$^+$ number flux ratios are presented in log scale in Figure 20 (right), including O$^+$/H$^+$ (top), O$^+$/He$^+$ (middle), and He$^+$/H$^+$ (bottom) flux ratios, where the solid lines represent the average flux ratios. Plots of O$^+$ versus H$^+$ fluxes (top), O$^+$ versus He$^+$ fluxes (middle), and He$^+$ versus H$^+$ fluxes (bottom) are shown in Fig-

ure 20 (left). The average O$^+$/H$^+$, He$^+$/O$^+$, and He$^+$/H$^+$ flux ratios were 0.06, 0.26, and 0.016. The average parallel number flux ratios were F_{He+} : F_{O+} : F_{H+} ~ 1 : 4 : 66, as summarized from Figure 20. The H$^+$ outflow was the dominant ion outflow at POLAR apogee, while O$^+$ was second, with a very low abundance of He$^+$. The average number flux ratios for three ion species are not the classical polar wind abundance relationship.

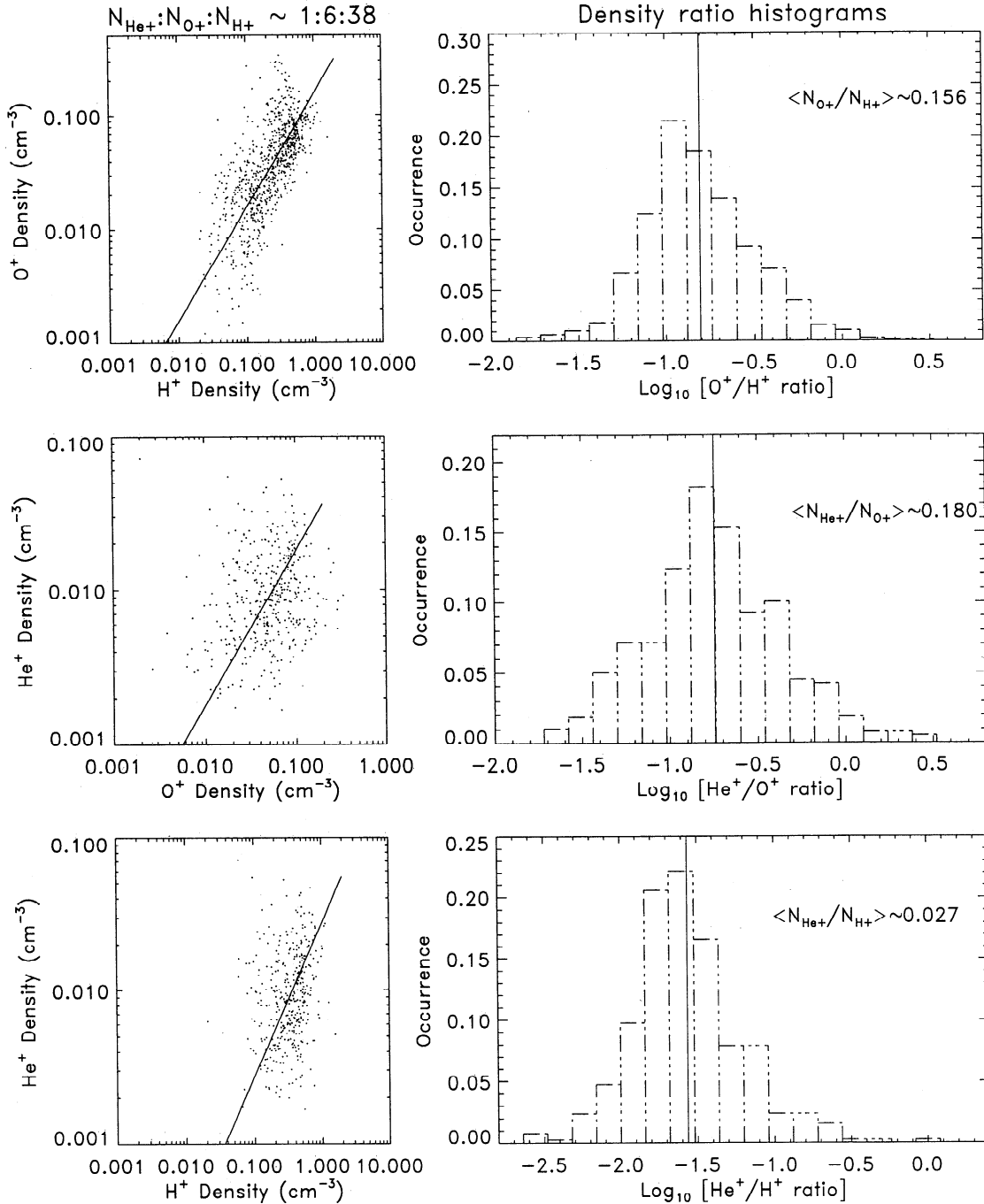Plots of the perpendicular versus parallel temperature for

$N_{He+}:N_{O+}:N_{H+} \sim 1:6:38$

Density ratio histograms

Figure 18. (left, top) O^+ versus H^+ density, (middle) He^+ versus O^+ density, and (bottom) He^+ versus H^+ density. (right, top) O^+/H^+, (middle) He^+/O^+, and (bottom) He^+/H^+ density ratio histograms in log scale. The solid lines represent the average density ratios.

H^+ (top) and O^+ (bottom) are shown in Figure 21 (left), and the parallel/perpendicular temperature ratio histograms are shown in log scale in Figure 21 (right), where the solid lines represent the average temperature ratios. At POLAR apogee, the average parallel/perpendicular temperature ratios $T_\parallel/T_\perp$ were $\sim$ 1.4 for H^+ and 1.9 for O^+. The parallel temperatures were higher than the perpendicular temperatures for both H^+ and O^+ ions, $T_{\parallel i} > T_{\perp i}$, which is opposite from the behavior of the ion temperatures at 5000 km altitude. This is presumably because of the effects of conversion of perpendicular to parallel energy

associated with (partial) conservation of the first adiabatic invariant along the diverging magnetic field lines.

In Figure 22, plots of the O^+ versus H^+ temperatures (left) are shown and the O^+/H^+ temperature ratio histograms (right) are shown, where the solid lines represent the average O^+/H^+ temperature ratios in both parallel (top) and perpendicular (bottom) directions. The O^+ parallel temperature is $\sim$4.6 times the H^+ parallel temperature, on average, while the perpendicular O^+/H^+ temperature ratio was $\sim$ 3.4. O^+ ions have higher temperature than H^+ ions, $T_{O+} > T_{H+}$, in general. However, one
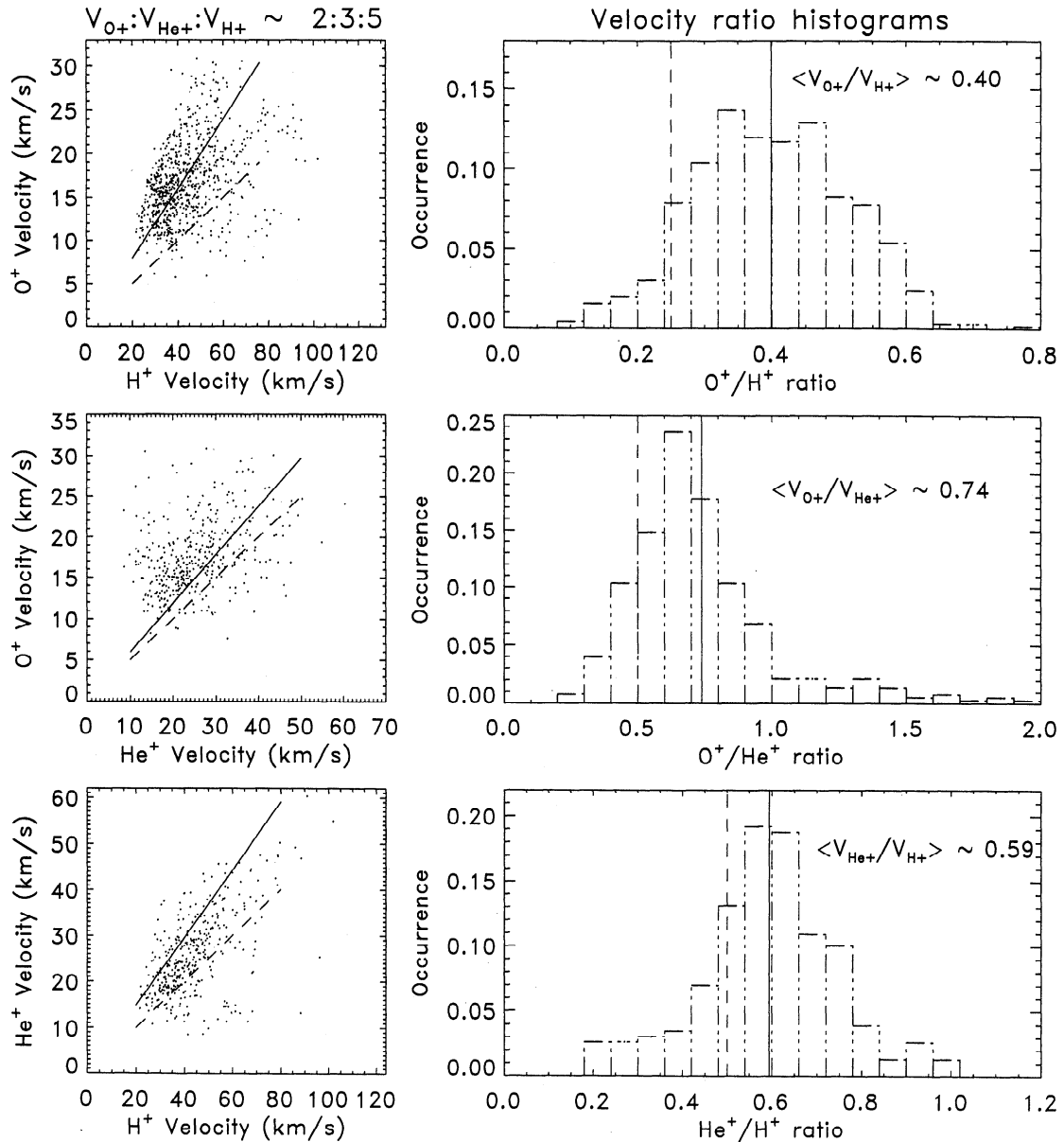
Figure 19. (left, top) O^+ versus H^+ velocity, (middle) O^+ versus He^+ velocity, and (bottom) He^+ versus H^+ velocity. (right, top) O^+/H^+, (middle) O^+/He^+, and (bottom) He^+/H^+ velocity ratio histograms. The solid lines represent the average parallel velocity ratios.

factor which could work to lower the O^+ temperatures would be velocity filtering from the narrow cleft ion fountain source [*Horwitz et al.*, 1985].

Figure 23 shows H^+ (top) and O^+ (bottom) parallel Mach number histograms at POLAR apogee, where the solid lines represent the average Mach numbers. The average H^+ Mach number was 4.6, ranging from ~ 2 to 7, and the average O^+ Mach number was 3.5, ranging from ~1 to 8. Both H^+ and O^+ flows were supersonic outflows at these high altitudes.

4.2. Relationship With Day-Night Distance in Solar Magnetic Coordinates at 8 R_E Altitude

The average bulk flow velocity ratios, $V_{O+} : V_{He+} : V_{H+}$ ~ 2 : 3 : 5, summarized from section 4.1, may suggest the importance of comparable energy gains for the ion species. However, the

individually observed velocity ratios span a wide range and may be consistent with varying contributions of such effects as gravitational force, velocity filter, centrifugal acceleration, and electrostatic acceleration in the transport of polar wind. In order to reveal further aspects of the high-altitude bulk parameters, Figures 24a and 24b show the O^+ and H^+ ion densities (top), parallel bulk velocities (middle), and parallel temperatures (bottom) versus X_{SM}. The ion densities decrease from the nightside to the dayside for three ion species, O^+, H^+, and He^+ (He^+ parameters versus X_{SM} are not shown here). Both O^+ and H^+ ion parallel velocities were higher on the dayside, and ion densities declined from nightside to dayside, which may suggest a cleft ion fountain origin. However, the parallel temperatures did not show the increasing trend from nightside to dayside, which might be expected for a cleft ion fountain origin for these ions [cf. *Horwitz and Lockwood*, 1985].
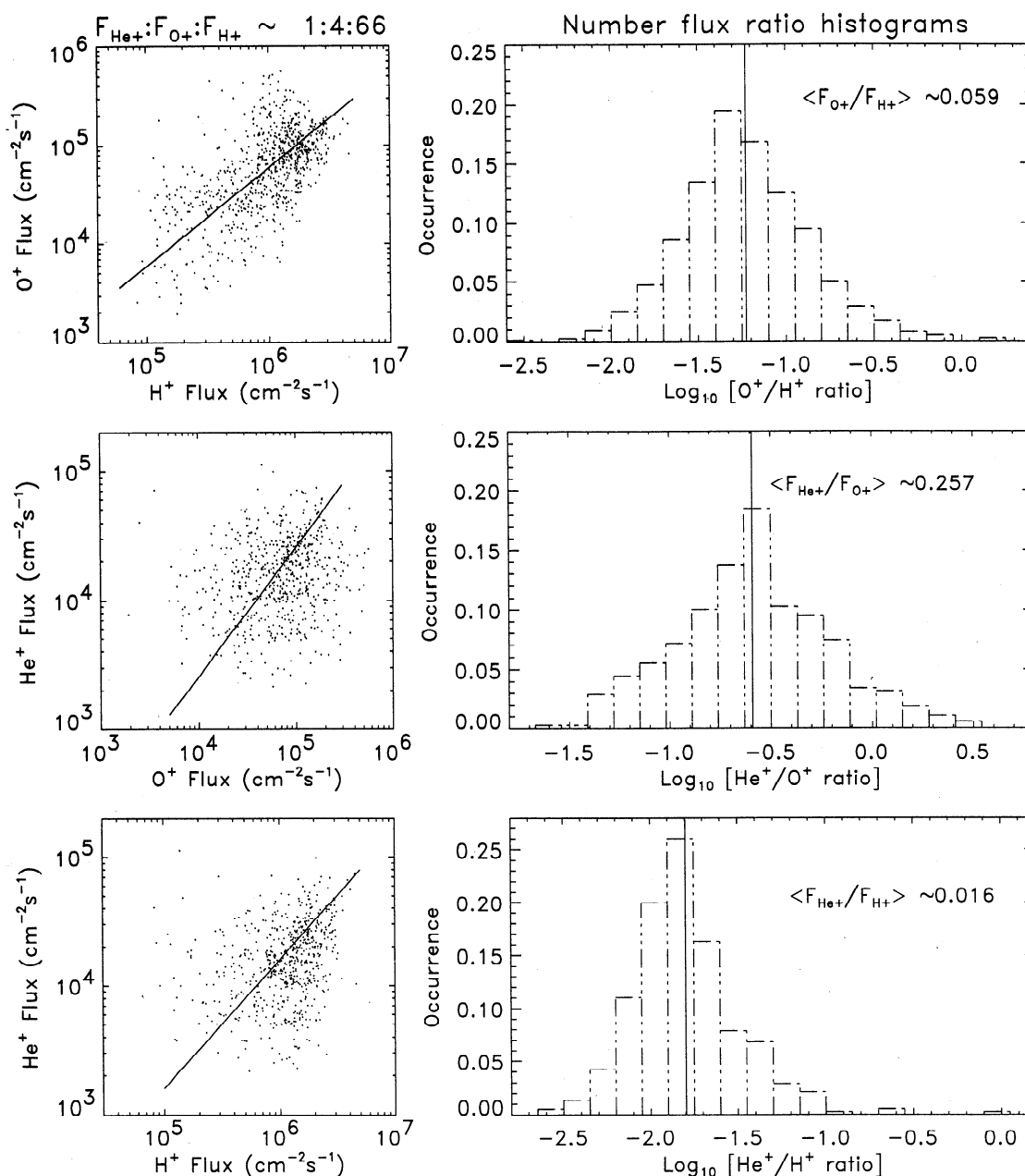
Figure 20. (left, top) O^+ versus H^+ number flux, (middle) He^+ versus O^+ number flux, and (bottom) He^+ versus H^+ number flux. (right, top) O^+/H^+, (middle) He^+/O^+, and (bottom) He^+/H^+ number flux ratio histograms. The solid lines represent the average number flux ratios.

5. Summary and Discussion

Apparent from this study are several significant characteristics of the polar wind at 5000 km and 8 R_E altitudes during April–May 1996.

1. The polar wind density is dominantly O^+ at 5000 km altitude but is strongly H^+ dominated at 8 R_E altitude. The He$^+$ ions play a very minor species in the polar wind.

2. The H^+ polar wind at 5000 km altitude is supersonic, with an average velocity of 15 km s^{-1}, while O^+ is subsonic, with an average velocity of −1 km s^{-1}, which is comparable with Akebono observations by *Abe et al.* [1993a, Figure 3]. At 8 R_E altitude, both H^+ and O^+ ion parallel flows are highly

supersonic. The H^+ ion outflow spans a broad bulk flow velocity range from 20 to 110 km s^{-1}, with an average velocity of ~ 45 km s^{-1}, while O^+ ion velocities ranged from 8 to 32 km s^{-1}, with an average velocity of ~ 27 km s^{-1}, which is faster than that predicted by some polar wind models [e.g., *Gombosi and Killeen*, 1987; *Wilson et al.*, 1990; *Demars and Schunk*, 1991; *Ho et al.*, 1993].

3. The perpendicular temperature is higher than the parallel temperature at 5000 km altitude for both H^+ and O^+, which may suggest perpendicular ion heating though wave-particle interactions [e.g., *Ganguli and Palmadesso*, 1987; *Demars and Schunk*, 1987, 1989; *Chen and Ashour-Abdalla*, 1990; *Brown et al.*, 1991; *Barakat and Barghouthi*, 1994; *Demars*
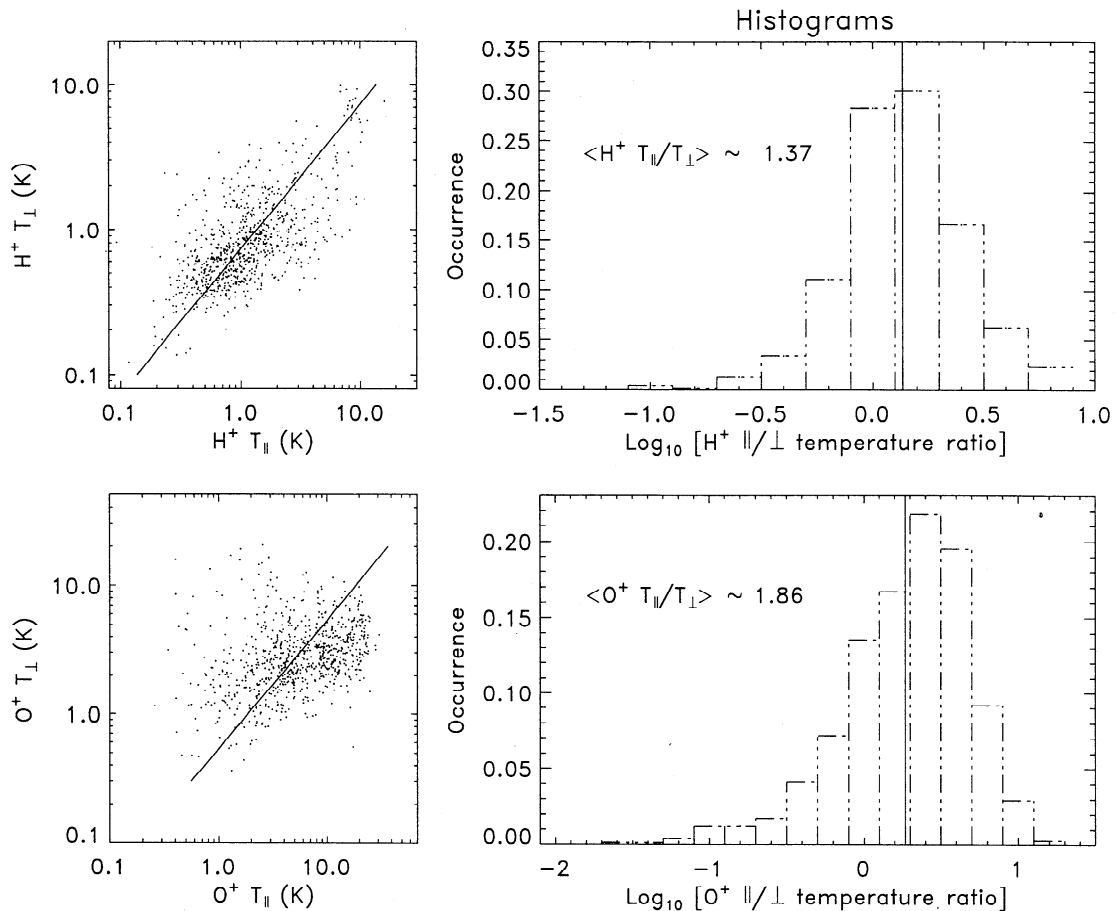
Figure 21. (right) Histograms of the occurrence frequency versus the parallel/perpendicular temperature ratios for (top) H^+ and (bottom) O^+ at 8 R_E altitude. (left) Parallel temperature versus perpendicular temperature for (top) H^+ and (bottom) O^+, with solid lines representing the average values.

et al., 1998]. At 8 R_E altitude, the parallel temperature is higher than the perpendicular temperature, which is likely due to the adiabatic conversion of perpendicular to parallel energy in the outward flow along the diverging magnetic field lines. The high-altitude ion temperature anisotropy, $T_{\parallel i} > T_{\perp i}$, is presumably due to the (partial) conservation of the magnetic moment and is consistent with various polar wind calculations [e.g., *Schunk and Watkins,* 1982; *Ganguli et al.,* 1987; *Demars and Schunk,* 1987, 1989, 1994], while at low altitudes, the ion temperature anisotropies are reversed to $T_{\perp i} > T_{\parallel i}$ as noted above.

4. The O^+ temperatures are higher than the H^+ temperatures at both low and high altitudes. The observed ion temperatures are higher than those found in any of the modeling results, unless hot ions are put in at the bottom of the simulation.

Horwitz and Lockwood [1985] showed that energy separation should occur in the ions transported from the ionospheric cleft energization region as they are convected across the polar cap. This could lead to a region of divergent flow marking the boundary between escaping and gravitationally bound ions. Thus it is to be expected that O^+ of ionospheric origin should be observable moving both upward and downward along polar cap field lines. Our O^+ polar wind survey has indicated downflowing O^+ ions at 5000 km altitude and upflowing O^+ ions at 8 R_E altitude, which is consistent with the cleft ion fountain paradigm [*Horwitz and Lockwood,* 1985]. Sig-

nificant O^+ downflows in the polar cap were observed from DE 1 RIMS by *Chandler* [1995] and were also obtained using a global ionosphere polar wind model [*Schunk and Sojka,* 1997]. Our H^+ polar wind measurements showing supersonic characteristics (the Mach number ranged from 2.2 to 5) are consistent with DE 1 observations [*Nagai et al.,* 1984], which included Mach numbers ranging from 2.6 to 5.1, in general accord with "classical" polar wind model results [e.g., *Banks and Holzer,* 1969; *Lemaire and Scherer,* 1970].

Abe et al. [1993a, Figures 4 and 5] found that the ion velocity and temperature distributions from Akebono exhibited a day-to-night asymmetry. From our TIDE polar wind survey, the day-night asymmetry was seen only in densities, which decreased from dayside to nightside, but not the velocities and temperatures at low altitudes (see Figure 13). Our average O^+ velocity at 5000 km altitude, -1 km s^{-1}, is consistent with *Abe et al.* [1993a, Figure 3] results; however, our average H^+ velocity, 15 km s^{-1}, is somewhat higher than their average of $\sim$ 8 km s^{-1}. At Akebono apogee (10,000 km), the average velocity ratios for O^+, He^+, and H^+ were about 2 : 3.5 : 6, which is comparable to TIDE polar wind observations, V_{O+} : V_{He+} : V_{H+} $\sim 2 : 3 : 5$, at POLAR apogee. At an altitude of 8 R_E, the ion densities decline from nightside to dayside while the ion velocities are larger on the dayside. No significant trend is seen for temperatures (see Figure 24).

Dramatic decreases of the 5000 km altitude H^+ and O^+ den-
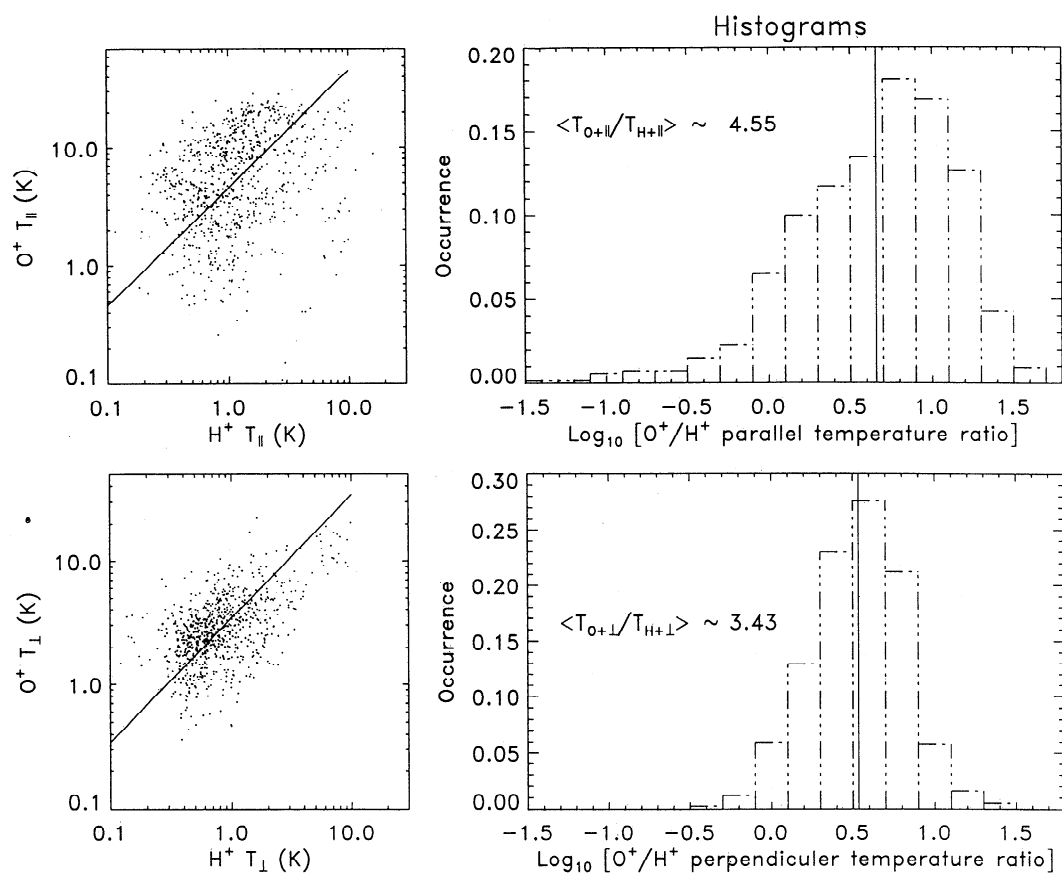
Figure 22. (right) Histograms of the occurrence frequency versus the O^+/H^+ (top) parallel and (bottom) perpendicular temperature ratios at 8 R_E altitude. (left) O^+ versus H^+ temperature for (top) parallel and (bottom) perpendicular component, with solid lines representing the average values.
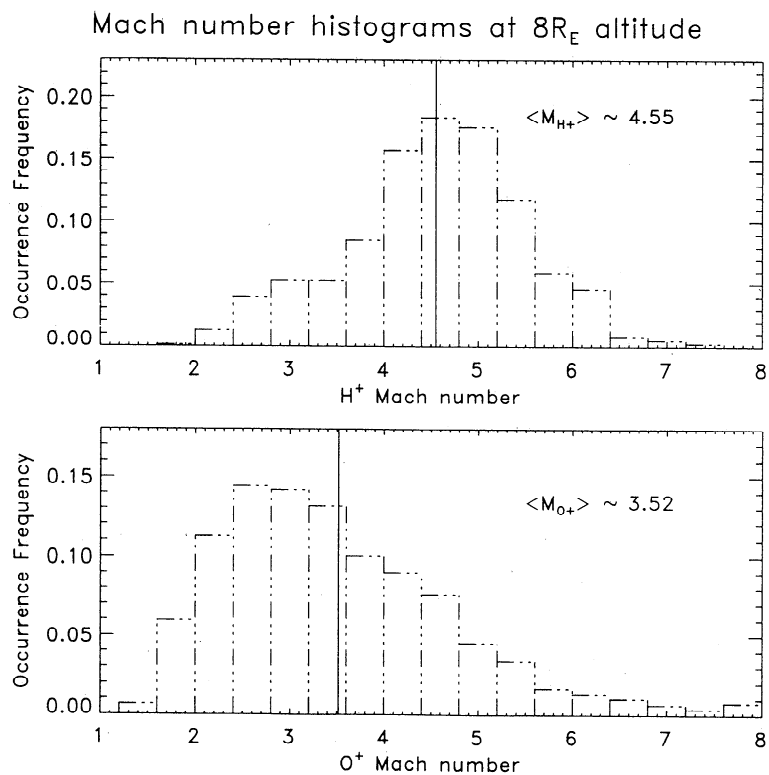

Figure 23. Parallel Mach number histograms for (top) H^+ and (bottom) O^+ at 8 R_E altitude, with solid lines representing the average Mach numbers.
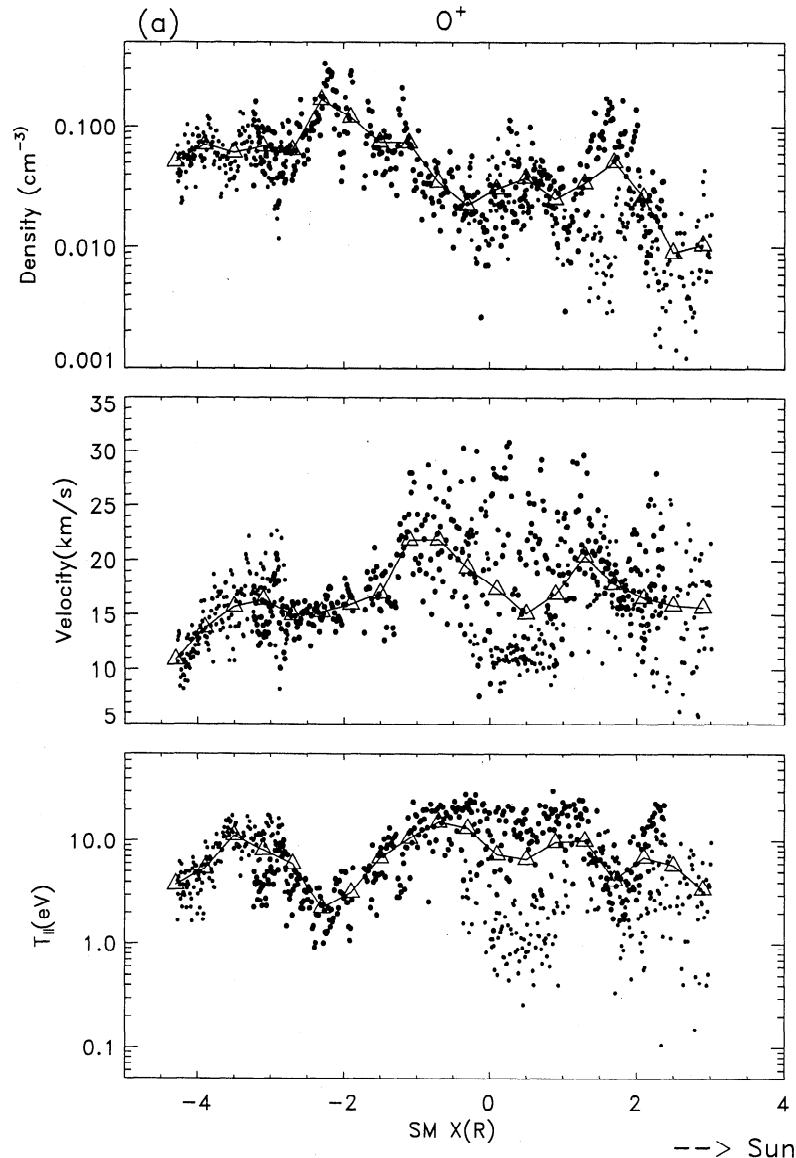
Figure 24. The (a) O^+ and (b) H^+ bulk parameters, including (top) density, (middle) velocity, and (bottom) parallel temperature, versus the X_{SM} at POLAR apogee. Open triangles are the average values over the interval of $0.4\ R_E$.

sities and fluxes are seen from 90° to 110° solar zenith angle for the ionospheric base. This is consistent with solar illumination ionization control. On the other hand, the downward O^+ flow and the O^+ densities decrease from dayside to nightside, which suggests the cleft ion fountain origin for the polar cap O^+ [*Lockwood et al.,* 1985a, b; *Horwitz and Lockwood,* 1985]. The O^+ densities are indeed highly correlated ($r = 0.98$) with X_{SM}. From our survey of the polar wind at low altitude, one conclusion would be that the solar zenith angle controls the H^+ polar wind in the polar cap, but the cleft ion fountain controls the polar cap O^+. The strongest evidence for cleft ion fountain control is actually the downward O^+ flow at 5000 km in polar cap. However, it may even be possible that the spread of cleft ion fountain O^+ influences the day-night variations of the H^+ polar wind as much or more than the direct solar illumination of the F region ionosphere, since the correlation coefficients for H^+ densities versus solar zenith angle and X_{SM} are similar, and the H^+ and O^+ densities are correlated with

a correlation coefficient $r = 0.8$ (shown in Figure 25). Enhanced upward flows of O^+ and enhanced O^+ densities in the cleft region are observed in the F region and topside ionosphere [e.g., *Loranc et al.,* 1991]. These would lead to enhanced O^+ extending from the cleft toward the center of the polar cap at altitudes down into the F region, which is where accidentally resonant charge exchange reaction, $O^+ + H \rightarrow H^+ + O$, takes place to produce ionospheric H^+. Thus the elevated densities of O^+ in the topside ionosphere (≤ 1000 km) toward the dayside (which could be partly associated with the cleft ion fountain processes) could indirectly also control the dayside increase of H^+ densities via this charge-exchange process within the low-altitude transition region. It will be interesting to further distinguish the cleft ion fountain and solar illumination controlling influences on the polar wind in further data analyses, as well as modeling investigations.

In addition to the polar wind characteristics and the relationship with SZA and X_{SM}, we have also investigated the
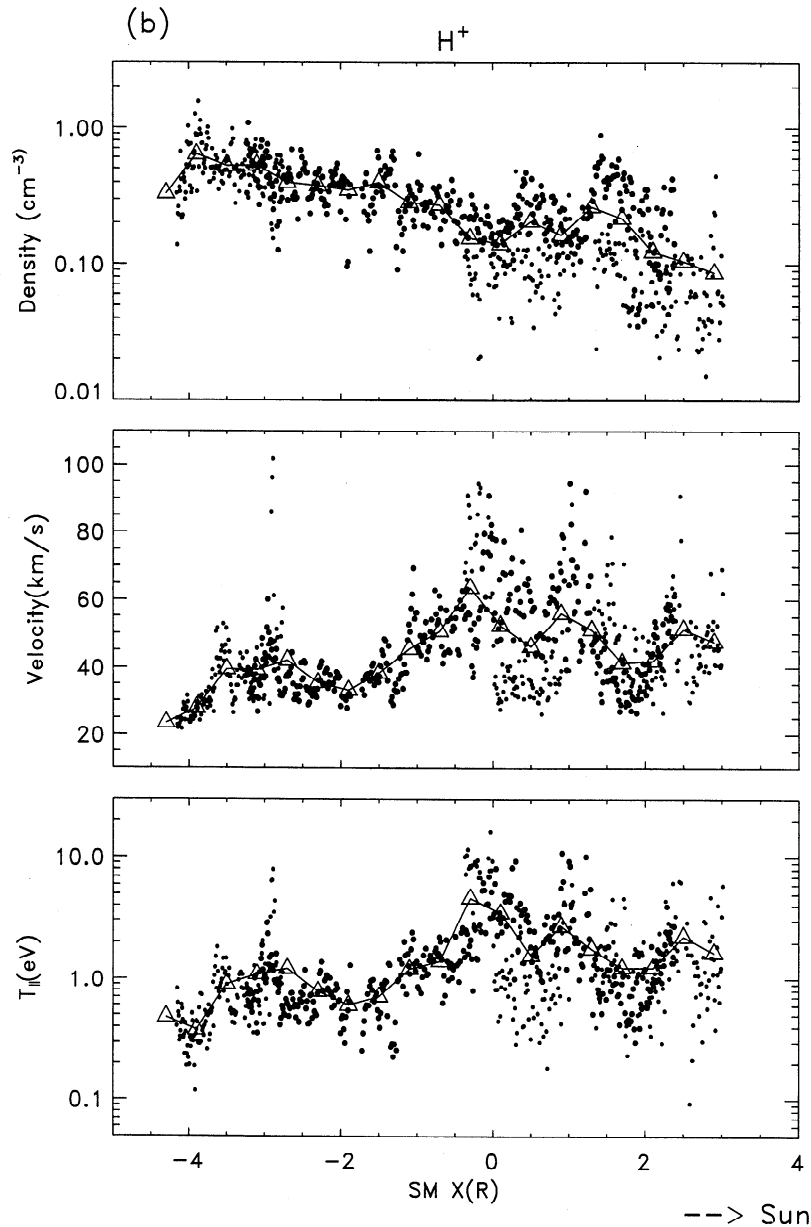
(b)

Figure 24. (continued)

possible relationship of the TIDE polar wind parameters with magnetic activity (e.g., Kp). No clear correlation which Kp was found from our survey (limited passes during April and May 1996). For the 20 perigee passes in April 1996, the Kp index varied between 1- and 5. Coincidentally, the higher Kp (3-5) appeared at low SZA (<100°) passes and the lower Kp (1-3) appeared at the high SZA passes. The Kp index was 3+ to 5 at POLAR apogee on April 19, 1996, and was 1- to 1 at apogee on May 28, 1996. Moreover, there is no clear relationship with the IMF B_z component, either. We conclude that the IMF and Kp produce no strong effect on the polar wind proper, on which we have based our polar wind measurements. Since we have used the more energetic particle signatures to restrict our measurements already to the polar cap field lines, regardless of the high-latitude auroral topology, it is not especially surprising that the physics of the polar wind might be insensitive to the IMF and Kp levels. On the other hand, we believe that O^+ ions at POLAR perigee are from the cleft

region, which could be influenced by the IMF and Kp. However, we find no strong correlation with IMF and Kp on O^+ flows at POLAR perigee.

H^+ and O^+ densities and O^+ number fluxes decrease from the dayside to the nightside with O^+ downward flow at 5000 km altitude. At 8 R_E altitude, H^+ and O^+ densities declined from the nightside to the dayside, while velocities increased from nightside to dayside. These may suggest cleft ion fountain origin. However, the "typical" parallel velocity ratios from TIDE high-altitude observations, V_{O+} : V_{He+} : $V_{H+} \sim 2 : 3 : 5$, may suggest the importance of comparable energy gains, such as via a photoelectron-driven electric potential layer. Several mechanisms for energizing and driving the polar plasma outflows have been studied, such as photoelectron effects [e.g., *Lemaire*, 1972; *Winningham and Gurgiolo*, 1982; *Horwitz et al.*, 1992; *Abe et al.*, 1993a, b; *Tam et al.*, 1995; *Yau et al.*, 1995; *Wilson et al.*, 1997; *Su et al.*, 1998], hot magnetospheric electrons, such as the polar rain, showers, and squall
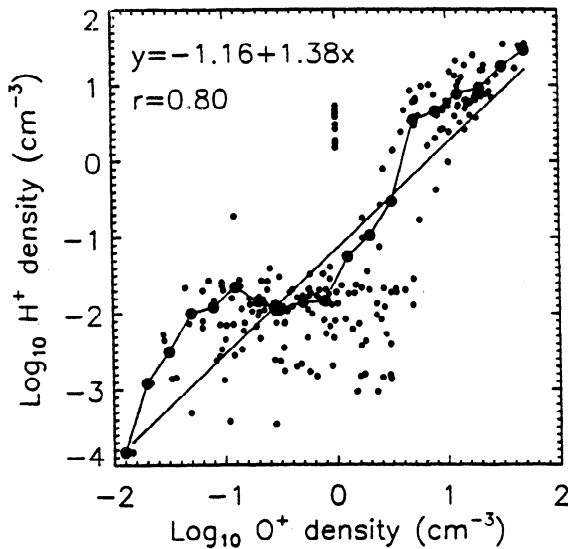
Figure 25. H$^+$ density versus O$^+$ density in log scale at POLAR perigee. Large solid circles with solid line are the average values; the straight line is the linear least squares fit in log scale with the correlation coefficient of 0.8.

[e.g., *Barakat and Schunk*, 1984; *Ho et al.*, 1992; *Su et al.*, 1998], and centrifugal acceleration associated with convection [e.g., *Cladis*, 1986; *Swift*, 1990; *Horwitz et al.*, 1994; *Demars et al.*, 1996].

Horwitz et al. [1994], using a steady state semikinetic model, demonstrated that centrifugal acceleration can be an ef-

fect of zeroth-order importance in describing the convecting polar wind if convection is strong. The O$^+$ velocity at 8 R_E geocentric distance increased from 1 to 8, 30, and 60 km s^{-1} for ionospheric convection electric fields increasing from 0 to 10, 50, and 100 mV/m [*Horwitz et al.*, 1994, Figure 6], while the H$^+$ velocity increased to 36, 48, and 72 km s^{-1} [*Horwitz et al.*, 1994, Figure 5]. Our observed parallel velocities of the polar wind at 8 R_E altitude are generally comparable to their results when the convection (centrifugal force) was turned on. They further suggested that the field-aligned and convection flow energies would be equal if the streams were accelerated only by such a centrifugal force. This problem requires additional investigation [*Elliott et al.*, 1997].

A comparison of our range of observed parameters from POLAR/TIDE with the photoelectron-driven polar wind model of *Su et al.* [1998] (which includes an electric double layer-associated discontinuity near 3.5 R_E) and the "baseline" polar wind results by a coupled fluid-semikinetic transport simulation for solar minimum conditions is shown in Figure 26. The horizontal solid and dashed lines in Figure 26 (middle and right) are the observed ranged of parallel velocities and densities from TIDE observations for H$^+$ and O$^+$ ions, respectively, at 5000 km and 8 R_E altitudes. The polar wind densities and parallel velocities from TIDE observations are comparable to the *Su et al.* [1998] simulation results, in general. The H$^+$/O$^+$ parallel velocity ranges observed by TIDE extend from the baseline polar wind value up to and beyond that of the photoelectron-driven polar wind velocity at 8 R_E altitude. This may indicate variations of the photoelectron fluxes from the ionosphere or downward magnetospheric electrons
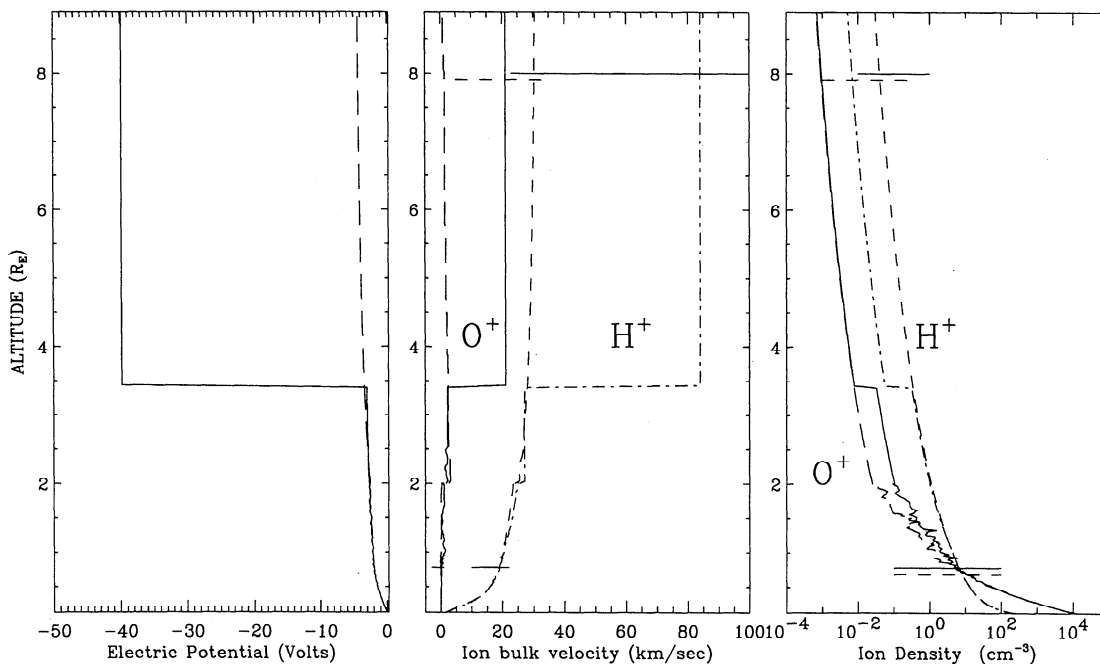

Figure 26. Comparison of survey parameter ranges with photoelectron-driven polar wind (solar minimum conditions) from 120 km to 9 R_E altitude [*Su et al.*, 1998]. (left) Electric potential, with the solid line representing the potential with photoelectron effects and the dashed line representing the baseline polar wind case. (middle) Ion bulk velocities and (right) densities. The solid and dot-dashed lines represent the O$^+$ and H$^+$ profiles for photoelectron-driven polar wind case, while the long-dashed and short-dashed lines are for the baseline polar wind case (no photoelectron effects included). The horizontal solid and dashed lines present the range of TIDE observed polar wind characteristics for H$^+$ and O$^+$ at 5000 km and 8 R_E altitude.

(such as polar rain, showers, squalls). Such variations could cause the suggested electrostatic double layer to vary in amplitude and altitude. *Persoon et al.* [1983] indicated the electron density variations in the polar cap from DE 1 plasma wave observations. *Barakat and Schunk* [1983, 1984] and *Ho et al.* [1992], using semikinetic simulations, also indicated that the polar wind outflows vary with electron temperature and density. More recently, *Barakat et al.* [1997] presented O^+ density and velocity variations at high altitudes using a time-dependent semikinetic polar wind simulation, including hot electron effects, with the ionospheric conditions input from a low-altitude ionosphere-atmosphere model [*Schunk and Sojka*, 1989]. Therefore it would be useful to analyze low-energy electron data from the HYDRA instrument on POLAR and examine the possible effects of the polar rain and photoelectrons. Combining the TIDE polar wind observations with HYDRA electron data may assist in understanding the large variation in the ion parallel flow velocities observed at very high altitudes.

The survey results to date are consistent with the concept derived from Dynamics Explorer (DE) 1 of a "fountain in a wind" of O^+ and more energetic light ions emanating from the dayside auroral oval, while also exhibiting characteristics that are familiar from theoretical descriptions of a thermal polar wind, independent of any auroral energy inputs. The survey clearly indicates a direction for future polar wind modeling studies, which should account for the closed circulation of polar plasma tubes with auroral energy inputs upon passage through the dayside and nightside auroral zones. A general simulation could be performed in which a particular flux tube is followed through a full convection cycle as an open flux tube convecting over the polar cap. The flux tube could be then allowed to close into an extended closed flux tube which convects into the auroral zone plasma sheet through the dusk or dawn magnetosphere. It would eventually convect back through the cleft/cusp region before again becoming an open flux tube in the polar region [e.g., *Schunk and Sojka*, 1989, 1997; *Demars et al.*, 1996, 1998].

References

Abe, T., B. A. Whalen, A. W. Yau, R. E. Horita, S. Watanabe, and E. Sagawa, EXOS D (Akebono) suprathermal mass spectrometer observations of the polar wind, *J. Geophys. Res., 98*, 11,191, 1993a.

Abe, T., B. A. Whalen, A. W. Yau, S. Watanabe, E. Sagawa, and K. I. Oyama, Altitude profile of the polar wind velocity and its relationship to ionospheric conditions, *Geophys. Res. Lett., 20*, 2825, 1993b.

Acuña, M. H., K. W. Ogilvie, D. N. Baker, S. A. Curtis, D. H. Fairfield, and W. H. Mish, The global geospace science program and its investigations, *Space. Sci. Rev., 71*(1-4), 21, 1995.

Banks, P. M., and T. E. Holzer, Features of plasma transport in the upper atmosphere, *J. Geophys. Res., 74*, 6304, 1969.

Barakat, A. R., and I. A. Barghouthi, The effect of wave-particle interaction on the polar wind O^+, *Geophys. Res. Lett., 21*, 2279, 1994.

Barakat, A. R., and R. W. Schunk, O^+ ions in the polar wind, *J. Geophys. Res., 88*, 7887, 1983.

Barakat, A. R., and R. W. Schunk, Effect of hot electrons on the polar wind, *J. Geophys. Res., 89*, 9771, 1984.

Barakat, A. R., H. G. Demars, and R. W. Schunk, Temporal behavior of the polar wind in the presence of hot electrons (abstract), *Eos Trans. AGU, 78*(46), Fall Meet. Suppl., F502, 1997.

Brinton, H. C., J. M. Grebowski, and H. G. Mayr, Altitude variation of ion composition in the midlatitude trough region: Evidence for upward plasma flow, *J. Geophys. Res., 76*, 3738, 1971.

Brown, D. G., G. R. Wilson, J. L. Horwitz, and D. L. Gallagher, "Self-consistent" production of ion conics on return current region auroral field lines: A time-dependent, semikinetic model, *Geophys. Res. Lett., 18*, 1841, 1991.

Chandler, M. O., Observations of downward moving O^+ in the polar topside ionosphere, *J. Geophys. Res., 100*, 5795, 1995.

Chandler, M. O., J. H. Waite Jr., and T. E. Moore, Observations of polar ion outflows, *J. Geophys. Res., 96*, 1421, 1991.

Chappell, C. R, T. E. Moore, and J. H. Waite Jr., The ionosphere as a fully adequate source of plasma for the Earth's magnetosphere, *J. Geophys. Res., 92*, 5896, 1987.

Chen, M. W., and M. Ashour-Abdallah, Heating of the polar wind due to ion beam instabilities, *J. Geophys. Res., 95*, 18,949, 1990.

Cladis, J. B., Parallel acceleration and transport of ions from polar ionosphere to plasma sheet, *Geophys. Res. Lett., 13*, 893, 1986.

Comfort, R. H., T. E. Moore, P. D. Craven, C. J Pollock, F. S. Mozer, and W. T. Williamson, Spacecraft potential control by PSI on the POLAR satellite, *J. Spacecr. and Rockets*, in press, 1998.

Demars, H. G., and R. W. Schunk, Temperature anisotropies in the terrestrial ionosphere and plasmasphere, *Rev. Geophys., 25*, 1659, 1987.

Demars, H. G., and R. W. Schunk, Solutions to bi-Maxwellian transport equations for the polar wind, *Planet. Space Sci., 37*, 85, 1989.

Demars, H. G., and R. W. Schunk, Comparison of semikinetic and generalized transport models of the polar wind, *Geophys. Res. Lett., 18*, 713, 1991.

Demars, H. G., and R. W. Schunk, A multi-ion generalized transport model of the polar wind, *J. Geophys. Res., 99*, 2215, 1994.

Demars, H. G., A. R. Barakat, and R. W. Schunk, Effect of centrifugal acceleration on the polar wind, *J. Geophys. Res., 101*, 24,565, 1996.

Demars, H. G., A. R. Barakat, and R. W. Schunk, Trapped particles in the polar wind, *J. Geophys. Res., 103*, 419, 1998.

Dessler, A. J., and P. A. Cloutier, Discussion of letter by Peter M. Banks and Thomas E. Holzer, "The polar wind," *J. Geophys. Res., 74*, 3730, 1969.

Elliott, H. A., et al., Ion outflow and convection in the polar cap and cleft as measured by TIDE, EFI, MFE, and TIMAS on POLAR (abstract), *Eos Trans. AGU, 78*(46), Fall Meet. Suppl., F623, 1997.

Ganguli, S. B., The polar wind, *Rev. Geophys., 34*, 311, 1996.

Ganguli, S. B., and P. J. Palmadesso, Plasma transport in the auroral return current region, *J. Geophys. Res., 92*, 8673, 1987.

Ganguli, S. B., H. G. Mitchell, and P. J. Palmadesso, Behavior of ionized plasma in the high latitude topside ionosphere: The polar wind, *Planet. Space Sci., 35*, 703, 1987.

Gombosi, T. I., and T. L. Killeen, Effects of thermospheric motions on the polar wind: A time-dependent numerical study, *J. Geophys. Res., 92*, 4725, 1987.

Gombosi, T. I., and R. W. Schunk, A comparative study of plasma expansion events in the polar wind, *Planet. Space Sci., 36*, 753, 1988.

Gombosi, T. I., T. E. Cravens, and A. F. Nagy, A time-dependent theoretical model of the polar wind: Preliminary results, *Geophys. Res. Lett., 12*, 167, 1985.

Gurgiolo, C., and J. L. Burch, DE-1 observations of the polar wind — A heated and an unheated component, *Geophys. Res. Lett., 9*, 945, 1982.

Gurnett, D. A., et al., The Polar Plasma Wave Instrument, *Space Sci. Rev., 71*(1-4), 597, 1995.

Harvey, P. J., et al., The electric field instrument on the POLAR spacecraft, *Space Sci. Rev., 71*(1-4), 583, 1995.

Ho, C. W., J. L. Horwitz, G. R. Wilson, N. Singh, and T. E. Moore, Effects of magnetospheric electrons on polar plasma outflow: A semikinetic model, *J. Geophys. Res., 97*, 8425, 1992.

Ho, C. W., J. L. Horwitz, N. Singh, and G. R. Wilson, Plasma expansion of density perturbations in the polar wind: comparison of semikinetic and transport models, *J. Geophys. Res., 98*, 13,581, 1993.

Hoffman, J. H., Studies of the composition of the ionosphere with a

magnetic deflection mass spectrometer, *Int. J. Mass Spectrom. Ion Phys., 4*, 315, 1970.

Hoffman, J. H., and W. H. Dodson, Light ion concentrations and fluxes during magnetically quiet times, *J. Geophys. Res., 85*, 626, 1980.

Hoffman, J. H., W. H. Dodson, C. R. Lippincott, and H. D. Hammack, Initial ion composition results from ISIS 2 satellite, *J. Geophys. Res., 79*, 4246, 1974.

Horwitz, J. L., The ionosphere as a source for magnetospheric ions, *Rev. Geophys., 20*, 929, 1982.

Horwitz, J. L., Features of ion trajectories in the polar magnetosphere, *Geophys. Res. Lett., 11*, 1111, 1984.

Horwitz, J. L., Core plasma in the magnetosphere, *Rev. Geophys., 25*, 579, 1987.

Horwitz, J. L., The ionosphere's wild ride in outer space, *Rev. Geophys., 33*, 703, 1995.

Horwitz, J. L., and M. Lockwood, The cleft ion fountain: A two-dimensional kinetic model, *J. Geophys. Res., 90*, 9749, 1985.

Horwitz, J. L., and T. E. Moore, Four contemporary issues concerning ionospheric plasma flow to the magnetosphere, *Space Sci. Rev., 80*, 49, 1997.

Horwitz, J. L., J. H. Waite Jr., and T. E. Moore, Supersonic ion outflows in the polar magnetosphere via the geomagnetic spectrometer, *Geophys. Res. Lett., 12*, 757, 1985.

Horwitz, J. L., C. J. Pollock, T. E. Moore, W. K. Peterson, J. L. Burch, J. D. Winningham, J. D. Craven, L. A. Frank, and A. Persoon, The polar cap environment of outflowing O^+, *J. Geophys. Res., 97*, 8361, 1992.

Horwitz, J. L., C. W. Ho, H. D. Scarbro, G. R. Wilson, and T. E. Moore, Centrifugal acceleration of the polar wind, *J. Geophys. Res., 99*, 15,051, 1994.

Lemaire, J., Effect of escaping photoelectrons in a polar exospheric model, *Space Res., 12*, 1413, 1972.

Lemaire, J., and M. Scherer, Model of the polar ion-exosphere, *Planet. Space Sci., 18*, 103, 1970.

Lockwood, M., J. H. Waite Jr., T. E. Moore, J. F. E. Johnson, and C. R. Chappell, A new source of suprathermal O^+ ions near the dayside polar cap boundary, *J. Geophys. Res., 90*, 4099, 1985a.

Lockwood, M., M. O. Chandler, J. L. Horwitz, J. H. Waite Jr., T. E. Moore, and C. R. Chappell, The cleft ion fountain, *J. Geophys. Res., 90*, 9736, 1985b.

Loranc, M., W. B. Hanson, R. A. Heelis, and P.-P. St.-Maurice, A morphological study of vertical ionospheric flows in the high-latitude *F* region, *J. Geophys. Res., 96*, 3627, 1991.

Moore, T. E., and D. C. Delcourt, The geopause, *Rev. Geophys., 33*, 175, 1995.

Moore, T. E., C. J. Pollock, R. L. Arnoldy, and P. M. Kintner, Preferential O^+ heating in the topside ionosphere, *Geophys. Res. Lett., 13*, 901, 1986a.

Moore. T. E., M. Lockwood, M. O. Chandler, J. H. Waite Jr., C. R. Chappell, A. Persoon, and M. Sugiura, Upwelling O^+ ion source characteristics, *J. Geophys. Res., 91*, 7019, 1986b.

Moore, T. E., et al., The thermal ion dynamics experiment and plasma source instrument, *Space Sci. Rev., 71*(1-4), 409, 1995.

Moore, T. E., M. O. Chandler, C. J. Pollock, D. L. Reasoner, R. L. Arnoldy, B. Austin, P. M Kintner, and J. Bonnell, Plasma heating and flow in an auroral arc, *J. Geophys. Res., 101*, 5279, 1996.

Moore, T. E., et al., High altitude observations of the polar wind, *Science, 277*, 349, 1997.

Nagai, T., J. H. Waite Jr., J. L. Green, C. R. Chappell, R. C. Olsen, and R. H. Comfort, First measurements of supersonic polar wind in the polar magnetosphere, *Geophys. Res. Lett., 11*, 669, 1984.

Olsen, R. C., C. R. Chappell, and J. L. Burch, Aperture plane potential control for thermal ion measurements, *J. Geophys. Res., 91*, 3117, 1986.

Persoon, A. M., D. A. Gurnett, and S. D. Shawhan, Polar cap electron densities from DE 1 plasma wave observations, *J. Geophys. Res., 88*, 10,123, 1983.

Pollock, C. J., M. O. Chandler, T. E. Moore, J. H. Waite Jr., C. R. Chappell, and D. A. Gurnett, A survey of upwelling ion event characteristics, *J. Geophys. Res., 95*, 18,969, 1990.

Raitt, W. J., R. W. Schunk, and P. M. Banks, A comparison of the temperature and density structure in the high and low speed thermal proton flows, *Planet. Space Sci., 23*, 1103, 1975.

Schunk, R. W., and J. J. Sojka, A three-dimensional time-dependent model of the polar wind, *J. Geophys. Res., 94*, 8973, 1989.

Schunk, R. W., and J. J. Sojka, Global ionosphere-polar wind system during changing magnetic activity, *J. Geophys. Res., 102*, 11,625, 1997.

Schunk, R. W., and D. S. Watkins, Electron temperature anisotropy in the polar wind, *J. Geophys. Res., 86*, 91, 1981.

Schunk, R. W., and D. S. Watkins, Proton temperature anisotropy in the polar wind, *J. Geophys. Res., 87*, 171, 1982.

Shelley, E. C., W. K. Peterson, A. G. Ghielmetti, and J. Geiss, The polar ionosphere as a source of energetic magnetospheric plasma, *Geophys. Res. Lett., 9*, 941, 1982.

Su, Y.-J., J. L. Horwitz, G. R. Wilson, P. G. Richards, D. G. Brown, and C. W. Ho, Self-consistent simulation of the photo-electron-driven polar wind from 120 km to 9 R_E altitude, *J. Geophys. Res., 103*, 2279, 1998.

Swift, D. W., Simulation of the ejection of plasma from the polar ionosphere, *J. Geophys. Res., 95*, 12,103, 1990.

Tam, S. W. Y., F. Yasseen, T. Chang, and S. B. Ganguli, Self-consistent kinetic photoelectron effects on the polar wind, *Geophys. Res. Lett., 22*, 2107, 1995.

Waite, J. H., Jr., T. Nagai, J. F. E. Johnson, C. R. Chappell, J. L. Burch, T. L. Killeen, P. B. Hays, G. R. Carignan, W. K. Peterson, and E. G. Shelley, Escape of suprathermal O^+ ions in the polar cap, *J. Geophys. Res., 90*, 1619, 1985.

Wilson, G. R., Semikinetic modeling of the outflow of ionospheric plasma through the topside collisional to collisionless transition region, *J. Geophys. Res., 97*, 10,551, 1992.

Wilson, G. R., C. W. Ho, J. L. Horwitz, N. Singh, and T. E. Moore, A new kinetic model for time-dependent polar plasma outflow: Initial results, *Geophys. Res. Lett., 17*, 263, 1990.

Wilson, G. R., G. Khazanov, and J. L. Horwitz, Achieving zero current on open flux tubes carrying large photoelectron fluxes, *Geophys. Res. Lett., 24*, 1183, 1997.

Winningham, J. D., and C. Gurgiolo, DE-2 photoelectron measurements consistent with a large scale parallel electric field over the polar cap, *Geophys. Res. Lett., 9*, 977, 1982.

Yau, A. W., B. A. Whalen, W. K. Peterson, and E. G. Shelley, Distribution of upflowing ionospheric ions in the high-altitude polar cap and auroral ionosphere, *J. Geophys. Res., 89*, 5507, 1984.

Yau, A. W., T. Abe, T. Chang, T. Mukai, K. I. Oyama, and B. A. Whalen, Akebono observations of electron temperature anisotropy in the polar wind, *J. Geophys. Res., 100*, 17,451, 1995.

M. O. Chandler and P. D. Craven, Space Sciences Laboratory, Marshall Space Flight Center, Huntsville, AL 35812.

B. L. Giles and T. E. Moore, Laboratory for Extraterrestrial Physics, Goddard Space Flight Center, Greenbelt, MD 20771.

M. Hirahara, Department of Physics, Rikkyo University, Tokyo 171, Japan.

J. L. Horwitz, Center for Space Plasma and Aeronomic Research, The University of Alabama in Huntsville, Huntsville, AL 35899.

C. J. Pollock, Instrumentation and Space Research Division, Southwest Research Institute, San Antonio, TX 78238.

Y.-J. Su, Space and Atmospheric Sciences, Los Alamos National Laboratory, Los Alamos, NM 87545. (e-mail: ysu@lanl.gov)